Autophagy is Regulated by Mitochondrial Calcium Transporters NCLX and MCU

Vitor de Miranda Ramos[1]*, Julian D.C. Serna[1], Eloisa A. Vilas-Boas[1], João Victor Cabral-Costa[1], Fernanda M. da Cunha[2], Alicia J. Kowaltowski[1]*.

[1]Departamento de Bioquímica, Instituto de Química, Universidade de São Paulo, São Paulo, Brazil

[2]Departamento de Bioquímica, Escola Paulista de Medicina, Universidade Federal de São Paulo, Brazil

*Corresponding authors:

Vitor de Miranda Ramos (ramosvm@usp.br)

Alicia J Kowaltowski (alicia@iq.usp.br)

Keywords

Autophagy regulation; calcium transport; hepatocytes; mitochondria; MCU; NCLX.

Abstract

Autophagy is responsive to intracellular signals, including calcium (Ca^{2+}) ions. Mitochondrial Ca^{2+} transporters such as the mitochondrial calcium uniporter (MCU, an uptake pathway) and $Na^{+}/Li^{+}/Ca^{2+}$ exchanger (NCLX, an efflux pathway) are known to shape Ca^{2+} signals within the cell, thereby regulating Ca^{2+}-sensitive cellular processes. However, the interplay between MCU, NCLX, and autophagy is unknown, and investigating the crosstalk between these important metabolic and signaling nodes was the aim of this study. We evaluated autophagic activity using a wide array of experimental approaches after siRNA-mediated MCU or NCLX knockdown. Under nutrient replete conditions, reduced expression of either NCLX or MCU led to decreased autophagic activity as well as altered expression of several autophagy-related genes, without affecting mitochondrial ATP synthesis. The knockdown of NCLX resulted in marked reduction of LC3 expression and of activation of the AMPK-UKL1 pathway. Interestingly, NCLX expression was increased under autophagy-promoting conditions *in vitro* and *in vivo,* demonstrating it is both regulatory of and regulated by autophagic stimuli. Also, genetic and pharmacological inhibition of NCLX caused impaired autophagosome formation and reduced autophagic flux after serum and amino acid starvation. In conclusion, our results uncover an important role for mitochondrial Ca^{2+} transport as a regulator of both basal and stimulated autophagic activity, modulating both autophagic initiation and autophagossome formation.

Abbreviations

AMPK: AMP-activated protein kinase; ATG: autophagy-related; BafA1: Bafilomycin A1; CGP: CGP 37157; CM: complete media; ER: endoplasmic reticulum; HBSS: Hanks' balanced salt solution; KD: knockdown; LC3: membrane-bound microtubule-associated protein light chain 3; mTORC1: mammalian target of rapamycin complex 1; MCU: mitochondrial calcium uniporter; NCLX: mitochondrial $Na^{+}/Li^{+}/Ca^{2+}$ exchanger; ULK1: Unc-51 like autophagy activating kinase 1.

Introduction

Autophagy is a conserved intracellular pathway that results in lysosomal degradation of a cell´s own components. In macroautophagy (which we will refer to as autophagy from now on), these components are selectively or non-selectively sequestered by autophagosomes, which in turn fuse with lysosomes to promote the digestion of cargo such as organelles or proteins [1]. Due to its ability to remove unwanted elements and promote specific or general nutrient availability, autophagy is necessary for quality control, tissue renovation, and metabolic regulation [1,2].

Autophagy levels have direct links to cell metabolism, as it promotes adaptive metabolic responses and, conversely, displays regulatory features which are highly sensitive to nutrients and metabolic signals [2,3]. Within this context, calcium (Ca^{2+}) ions are well known second messengers in both metabolic and autophagic signaling [4,5]. For instance, the presence of amino acids or growth factors generates Ca^{2+} signals in the cytosol which are required for downstream effects, including the regulation of autophagy [6,7]. However, the genesis and consequences of Ca^{2+} signaling in the autophagic process are very context-dependent, and not yet well understood. This is intrinsically related to the fact that Ca^{2+} signals are shaped at subcellular levels by many ion transporters in different organelles, thus resulting in variable effects for most steps of the autophagy machinery. In fact, endeavors to investigate the role of specific Ca^{2+} transporters located in the endoplasmic reticulum (ER) or lysosome, rather than overall cellular Ca^{2+} levels, have strongly contributed to untangle particular aspects of autophagic regulation [8,9].

In line with this, mitochondria are capable to uptake, retain, and release Ca^{2+}, acting as cytosolic buffers for this ion, and thus shaping Ca^{2+} signals over time and within cellular microenvironments [10,11]. However, the contribution of transporters that promote Ca^{2+} uptake and efflux in mitochondria has been less studied in the context of autophagy.

The modulation of cytosolic Ca^{2+} signaling by mitochondria has been demonstrated in many different cell types and using a variety of experimental approaches [11-14]. Mitochondrial Ca^{2+} uptake is mediated by the mitochondrial calcium uniporter (MCU) [15,16]. MCU itself is the pore-

forming subunit in the MCU complex, which allows Ca^{2+} to enter the mitochondrial matrix in a manner dependent on the inner mitochondrial membrane potential ($\Delta\psi$). Other proteins forming the MCU complex regulate and support this transport [15]. Importantly, MCU activity is known to participate in several Ca^{2+}-dependent physiological processes such as cardiac function, insulin secretion, and inflammation [10]. In the context of autophagy regulation, inhibition of the MCU, under conditions in which ATP synthesis was hampered, has been associated with AMP-activated protein kinase (AMPK)-dependent activation of autophagy and mitophagy [17-19]. Other studies have observed that MCU activation may support mitophagy/autophagy instead [20-22], suggesting that more investigation is necessary, particularly under conditions in which mitochondrial Ca^{2+} transport is modulated without changes in oxidative phosphorylation.

Two specific transporters mediate Ca^{2+} efflux from mitochondria: a mitochondrial H^+/Ca^{2+} exchanger, which promotes electroneutral transport resulting in calcium extrusion, with a disputed molecular identity [10,23]; and the mitochondrial $Na^+/Li^+/Ca^{2+}$ exchanger (NCLX), that promotes transport by releasing matrix Ca^{2+} in exchange for Na^+ ions. After the identification of the NCLX gene in 2010 [24], several studies uncovered important functions of this transporter in a myriad of biological contexts. For example, inhibition of NCLX was shown to regulate insulin secretion, cardiomyocyte automaticity, and lactate and glutamate secretion in astrocytes, all by shaping Ca^{2+} signals [25-28]. Nonetheless, the participation of NCLX in autophagy regulation has not yet been investigated.

MCU and NCLX activity have been associated with a variety of pathological contexts in which autophagy also has a significant role, such as ischemia/reperfusion, heart failure, and Alzheimer's [29], demonstrating the need to investigate the interplay between these pathways. This work focused on investigating the impacts of changes in mitochondrial Ca^{2+} handling on autophagic activity and regulation, given that NCLX and MCU can shape cytosolic Ca^{2+} signals, and that autophagy regulation is sensitive to this ion. Specifically, we tested how inhibition of MCU or NCLX impact upon the levels of basal and stimulated autophagy. Our results provide insights into the

coordinated metabolic signaling that occurs between mitochondria and autophagy, uncovering mitochondrial Ca^{2+} transport as an important autophagic regulatory node.

Results

Mitochondrial Ca^{2+} transporters shape cytosolic Ca^{2+} signaling

We chose to study if mitochondrial Ca^{2+} transport regulates autophagy primarily in AML12 cells, a non-tumoral cell line derived from murine hepatocytes [30], given the importance and activity of autophagic processes in the liver. We tested if these cells presented the known effects of cytoplasmic Ca^{2+} concentrations on autophagy by treating them with 50 µM BAPTA-AM, an intracellular Ca^{2+} chelator. After 3 hours, BAPTA-AM significantly impacted autophagosome levels, as shown by the decrease in membrane-bound microtubule-associated protein light chain 3 (LC3) II levels (**Figure 1A**). This shows that autophagosome formation was decreased by Ca^{2+} chelation and confirms that cytosolic Ca^{2+} levels control autophagic machinery in AML12 cells.

Next, we promoted the genetic knockdown (KD) of mitochondrial Ca^{2+} transporters by transfecting with siRNAs targeting either NCLX (siNCLX), MCU (siMCU), or negative controls (siNC). Transfection with siNCLX resulted in a 55% mean reduction in NCLX mRNA levels after 48 hours of transfection, and 40% after 72 hours, compared to siNC (**Figure 1B**). NCLX protein forms (50 and 70 kDa, but not 100 kDa) were also decreased after 72 hours (**Figure 1C**). Transfection with siMCU resulted in 80% and 85% mean reduction of MCU mRNA levels 48 and 72 hours after transfection, respectively (**Figure 1D**). MCU protein levels were also significantly reduced 72 hours after transfection (**Figure 1E**).

To understand how Ca^{2+} handling by mitochondria was affected, we measured the capacity to take up and retain Ca^{2+} ions by these organelles 72 hours after transfection in digitonin-permeabilized cells, a condition in which the cytosol is diluted, and Ca^{2+} uptake is primarily mitochondrial [31]. Ca^{2+} uptake in mitochondria was followed by adding successive Ca^{2+} boluses and measuring

extramitochondrial concentrations, which decrease as the organelle uptakes the ion (**Figure 1F**). Interestingly, mitochondria with reduced NCLX or MCU expression showed increased maximum Ca^{2+} retention capacity compared to control cells (**Figure 1G**). Additionally, mitochondrial Ca^{2+} uptake rates were significantly reduced in siMCU cells, as expected (**Figure 1H**). Curiously, while NCLX expression was unchanged by MCU KD (Fig. S1A), we observed that NCLX KD led to a small increase in MCU mRNA and protein levels (Fig. S1B and C). However, this did not significantly affect Ca^{2+} uptake rates by these mitochondria, although some replicates showed a faster tendency (**Figure 1H -** paired replicates are indicated by symbol colors).

NCLX and MCU have both been shown to shape cytosolic Ca^{2+} signals in different types of cells [11]. We analyzed cytosolic Ca^{2+} levels through Fura-2 fluorescence ratios in intact siNCLX and siMCU AML12 cells upon stimulation with 100 µM ATP, which elicited a rapid increase in cytosolic Ca^{2+} concentrations, followed by a slower decay down to near-basal levels (**Figure 1I**). Interestingly, the ATP-induced Ca^{2+} peak was lower in siNCLX cells compared to siNC (**Figure 1J**), while in siMCU cells Ca^{2+} responses were similar to controls. The half-life decay time after the Ca^{2+} peak was significantly higher in siNCLX cells compared to siNC, suggesting that Ca^{2+} clearance pathways were impaired (**Figure 1K**). Although there was no significant change in siMCU cells, we observed a tendency toward an increase when comparing paired experiments (**Figure 1K**), thus indicating the participation of mitochondrial Ca^{2+} cycling in cytosolic Ca^{2+} buffering.

Basal autophagy is impaired by NCLX and MCU KD

We then investigated if basal autophagic activity in complete media (CM) was affected by NCLX and MCU KD by measuring LC3 I and II levels in the presence or absence of the lysosome inhibitor Bafilomycin A1 (BafA1), 72 hours after siRNA transfection (**Figure 2A**). We did not observe a significant difference between groups in the steady-state levels of LC3 II, measured in the absence of BafA1 (**Figure 2B**), but noted LC3 II accumulated after 1 hour in the presence of BafA1, as expected. This accumulation of LC3 II was lower in siNCLX and siMCU cells compared to siNC,

suggesting impaired autophagosome formation, demonstrating that changes in mitochondrial Ca^{2+} transport affect autophagic machinery.

Interestingly, LC3 I levels were also significantly reduced by siNCLX transfection, regardless of BafA1 presence, while there was no effect of siMCU (**Figure 2C**), indicating that NCLX affects the levels of autophagic signaling proteins, as well as their post-translational modifications. We also calculated the net flux LC3 II lysosomal degradation by comparing BafA1-treated and -untreated samples [32]. Both siNCLX and siMCU groups showed significantly reduced net flux compared to siNC (**Figure 2D**), demonstrating that mitochondrial Ca^{2+} transporters are indeed involved in the regulation of autophagic process.

Since we saw reduced LC3 I levels in siNCLX cells, we investigated whether the expression of LC3A and LC3B mRNAs was altered. In agreement with protein levels, LC3A mRNA was significantly reduced in siNCLX cells 48 and 72 hours after transfection (**Figure 2E**). Moreover, LC3B mRNA was also reduced at the 48 hours timepoint, but not at 72 hours. In siMCU cells, LC3A and LC3B mRNA expression was unchanged 48 hours after transfection, and only LC3A was reduced after 72 hours (**Figure 2E**). Interestingly, the expression of other autophagy-related genes, such as *Tfeb*, *Atg5*, and *Atg12* was increased by NCLX KD, suggesting that LC3 expression is regulated by a distinct pathway in this model (Fig S2A, C and D). Curiously, the expression of *Tfeb, Atg5*, and *Atg12* was also reduced in siMCU cells 72 hours after transfection, translating to reduced ATG12–ATG5 protein conjugate levels (Fig S2B, C and D).

As an additional strategy to study autophagy under basal conditions, we generated an AML12 cell line stably expressing mCherry-GFP-tagged LC3B (AML12-LC3 cells), which allows the visualization of autophagosomes ($mCherry^+/GFP^+$ puncta) and autolysosomes ($mCherry^+/GFP^-$ puncta) through fluorescence microscopy [32,33] (**Figure 2F**). Similar to the previous observation quantifying LC3 II, steady-state autophagosome levels were unchanged by KD of NCLX, but accumulation due to BafA1 treatment was reduced in these cells relative to controls (quantified in **Figure 2G**). Importantly, $mCherry^+/GFP^-$ puncta were significantly reduced in siNCLX cells

compared to siNC, regardless of BafA1 presence, suggesting that conversion of the autophagosome to an autolysosome is also impaired by the lack of NCLX. Unexpectedly, we did not observe significant changes in autophagosome and autolysosome puncta in siMCU cells compared to siNC, except for a slight increase in autophagosome levels in BafA1-treated cells (**Figure 2G**).

To comprehensively assess the effects of NCLX and MCU KD on autophagy, we also measured the levels of total polyubiquitinated proteins, which are substrates for autophagic degradation. Cells transfected with siNCLX presented a small, non-significant, decrease in total polyubiquitinated proteins, while siMCU cells displayed a significant increase in ubiquitinated proteins compared to siNC (**Figure 2H**). When the cells were treated with BafA1, NCLX KD led to lower accumulation of polyubiquitinated proteins, indicating that the machinery responsible for protein ubiquitination is inhibited in these cells (**Figure 2H**). An increased amount of polyubiquitinated proteins was not observed in siMCU cells treated with BafA1, which suggests that accumulation under basal conditions was due to decreased lysosomal degradation, rather than increased ubiquitination rates (**Figure 2I**). As a control, we measured proteasome activity (which is also responsible for the removal of polyubiquitinated proteins) and no significant changes were observed in NCLX or MCU KD cells (Fig. S3). Overall, these data indicate that KD of MCU and particularly NCLX can suppress autophagic activity under basal conditions.

NCLX KD suppresses ULK1 phosphorylation by AMPK

Since our data indicated that autophagosome formation was decreased by NCLX and MCU KD, we decided to investigate possible alterations promoted by changes in mitochondrial Ca^{2+} transport on initial autophagy steps, such as unc-51-like autophagy activating kinase 1 (ULK1) phosphorylation status, which is modulated by cellular nutrient signals and coordinates recruitment of downstream ATG proteins to the autophagosome formation site [34]. We measured the levels of total ULK1 and its phosphorylation by the nutrient sensor mammalian target of rapamycin complex 1 (mTORC1) at Ser757, and by AMPK at Ser555. Interestingly, total levels of ULK1 were sensitive

to the KD of both mitochondrial Ca^{2+} transporters: while siNCLX cells presented increased ULK1 protein levels, there was a decrease in siMCU cells (**Figure 3A**). mTORC1 can phosphorylate different ULK1 residues including Ser757, resulting in its inhibition and suppression of autophagy [43]. The levels of Ser757 phosphorylation presented a similar pattern to the total protein, which was increased in siNCLX cells and decreased in siMCU (**Figure 3B**). Thus, there was no significant alteration in the proportion of phosphorylation to total protein, suggesting that the activity of the mTORC1-ULK1 axis is unaltered (**Figure 3C**). In agreement, we also did not see changes in the phosphorylation of 4E-BP1 (**Figure 3D-F**), a downstream sensor of mTORC1 activity.

We also assessed the phosphorylation of ULK1 Ser555, one of the residues AMPK targets, promoting ULK1 activation and autophagic upregulation [34]. This residue was less phosphorylated in absolute quantities in siMCU cells (**Figure 3G**), and proportionally less phosphorylated in siNCLX cells (**Figure 3H**). Importantly, alterations in the AMPK-ULK1 pathway were not due to changes in ATP synthesis rates promoted by MCU or NCLX silencing, since ATP-linked oxygen consumption was unchanged cells under the conditions we adopted (**Figure 3I**, see [35]).

NCLX expression is increased during autophagic stimulus

Since we saw substantial effects of modulating the expression of mitochondrial Ca^{2+} transporters on basal autophagic activity, we questioned if NCLX and MCU were also modulators of autophagy in the context of its stimulation by nutritional deprivation. We began by analyzing if the expression of either NCLX or MCU was regulated by serum and amino acid deprivation using Hanks' balanced salt solution (HBSS) or the inhibition of mTORC1, one of the main nutrient deprivation sensors. We found that the levels of MCU mRNA were unaffected by HBSS and rapamycin treatment within 24 hours (**Figure 4A**). Conversely, NCLX expression was significantly increased from 6 to 24 hours after HBSS treatment (**Figure 4B**), an effect not seen with rapamycin treatment, suggesting that inhibition of mTORC1 alone is not sufficient to regulate NCLX expression. In agreement with mRNA quantifications in nutrient-deprived cells, we observed increased NCLX protein levels (of

both ~50 kDa and 100 kDa bands) in immunoblots of isolated liver mitochondria from mice that underwent 4 months of a caloric restriction (CR) diet compared to an *ad libitum* (AL) diet (**Figure 4C**). Overall, these data show that the expression of NCLX is highly sensitive to nutritional availability, and is upregulated under nutrient deprivation conditions known to promote autophagy.

NCLX KD impairs starvation and rapamycin-induced autophagy

Since NCLX expression was upregulated during nutrient deprivation, our next step was to investigate the effects of siNCLX on induced autophagy. We treated control siNC and siNCLX cells with HBSS (1 hour) or rapamycin (200 nM, 3 hours), measuring LC3 I and II levels as an autophagy readout. As expected, HBSS treatment increased LC3 II while reducing LC3 I levels, indicating LC3 lipidation and autophagy activation (**Figures 5A and B**). Under these conditions, KD of NCLX completely prevented LC3 II increase by HBSS. Importantly, LC3 II levels were also decreased by NCLX KD when BafA1 was present (**Figure 5C**), and LC3 II net flux during starvation was also reduced (**Figure 5D**), confirming overall induced autophagy inhibition by decreasing NCLX expression and activity. In agreement, AML12-LC3 cells transfected with siNCLX presented less autolysosome puncta ($mCherry^+/GFP^-$ puncta) when in HBSS (**Figure 5I**). Curiously, autophagosome puncta ($mCherry^+/GFP^+$ puncta) were similar between phenotypes under this condition. This may be related to the probe, inducing exogenous expression of LC3 protein in these cells, given that we observed a reduction in endogenous LC3 by siNCLX. Moreover, autophagy stimulation by rapamycin treatment was also impaired in siNCLX cells compared to siNC, as shown by decreased LC3 II in the absence or presence of BafA1 (**Figure 5E-G**), as well as reduced net flux (**Figures 5H**). Overall, these results comprehensively demonstrate that siNCLX cells are not able to upregulate autophagy upon nutritional withdrawal, and confirm this mitochondrial Ca^{2+}/ Na^+ exchanger is a strong regulator of autophagic induction and flux.

CGP 37157 inhibits NCLX activity and shapes cytosolic Ca^{2+} signaling

Chronic depletion of NCLX in KD cells may have secondary effects which can affect autophagy, so we decided to test if acute pharmacological inhibition of NCLX activity by its antagonist CGP 37157 (CGP) could also lead to autophagic regulation. Initially, we tested if treatment with 10 µM CGP was able to inhibit mitochondrial Ca^{2+} efflux by measuring the Ca^{2+} concentration within the mitochondrial matrix using the genetically-encoded probe, mito-GEM-GECO1 [36]. The addition of 100 µM ATP led to mitochondrial Ca^{2+} uptake, resulting in a rapid increase in intramitochondrial Ca^{2+} levels and a later slower decay towards basal levels (**Figure 6A, grey line**), corresponding to the efflux rate. Cells in the presence of CGP (**Figure 6A, blue line**) did not present a measurable efflux rate after ATP-generated Ca^{2+} peak, confirming that CGP acts as a specific NCLX inhibitor in our model, affecting mitochondrial Ca^{2+} extrusion, but not uptake upon ATP stimulation. We also measured cytosolic Ca^{2+} levels after ATP stimulation in the presence or absence of CGP (**Figure 6B**). CGP affected cytosolic Ca^{2+} clearance, as shown by a significant reduction in the half-life decay, without affecting the Ca^{2+} peak, probably due to more effective entrapment of the ion in mitochondria due to inhibition of its extrusion pathway.

Pharmacological NCLX inhibition suppresses starvation-induced autophagy

Next, we activated autophagy with HBSS or rapamycin in the presence of CGP to understand the effects of acute NCLX inhibition. Although the levels of steady-state LC3 II were increased by HBSS treatment, there were no significant effects of CGP compared to vehicle (DMSO) on this increase (**Figure 6C**). However, while HBSS led to a reduction of LC3 I, the presence of CGP led to LC3 I accumulation compared to DMSO (**Figure 6D**), suggesting that NCLX inhibition impaired LC3 I lipidation. In agreement, LC3 II levels in the presence of BafA1 were reduced in CGP-treated cells (**Figure 6E**), resulting in reduced LC3 II net flux (**Figure 6F**).

When cells were treated with rapamycin instead of HBSS to induce autophagy, we also did not observe an alteration in LC3 II steady-state levels by CGP (**Figure 6G**). Curiously, we saw a

small reduction in LC3 II steady-state levels by CGP in control cells (CM), which may indicate that longer NCLX inhibition (more than 3 hours) affects basal autophagy (**Figure 6G**). LC3 I levels were equal under basal conditions with or without CGP, but higher in the NCLX-inhibited cells when rapamycin was present (**Figure 6H**). Unexpectedly, LC3 II levels in the presence of BafA1 and LC3 II net flux were not significantly changed by CGP treatment during rapamycin-induced autophagy, suggesting that serum and amino acid starvation-induced autophagy is more sensitive to NCLX inhibition (**Figures 6I and J**).

Inhibition of mTORC1 is one of the main pathways involved in autophagic activation during serum and amino acid starvation. We then evaluated 4E-BP1 phosphorylation levels as a readout for mTORC1 activity to investigate if CGP could affect this pathway. As expected, the presence of HBSS and rapamycin led to a significant reduction in 4E-BP1 phosphorylation (**Figures 6K and L**). Interestingly, the presence of CGP partially suppressed HBSS effects, but not those of rapamycin. Thus, regulation of autophagy during serum and amino acid starvation may be more sensitive to NCLX inhibition due to the modulation of mTORC1 activity by CGP, which does not occur in rapamycin-induced autophagy.

Importantly, to test the involvement of intracellular Ca^{2+}, we measured LC3 II levels in cells pre-incubated with BAPTA-AM and then starved in the presence of either CGP or DMSO. As previously observed, pre-incubation with BAPTA-AM led to a significant reduction of LC3 II levels and an increase in LC3 I. Notably, CGP effects on LC3 I and II were not observed when intracellular Ca^{2+} was reduced by BAPTA-AM, confirming that changes in intracellular Ca^{2+} signaling are necessary for autophagy suppression by acute NCLX inhibition (**Figure 6M**).

Discussion

Autophagy, Ca^{2+}, and mitochondria participate in a myriad of homeostatic and signaling processes which are essential for cell survival and function. As central hubs in the regulation of complex signaling networks, their activities are expected to be coordinated, and to respond in a

coherent and integrated manner to environmental stimuli. Here, we specifically addressed the role of mitochondrial Ca^{2+} transporters in autophagy, and uncovered a new and important determinant of basal and stimulated autophagic activity. Our evidence that mitochondrial Ca^{2+} transport is a key player in autophagy includes experimental demonstrations that (i) the activity of MCU and NCLX, Ca^{2+} transporters in mitochondria, modulates intracellular Ca^{2+} signaling in hepatocyte-derived cells, a key regulator of autophagy; (ii) decreased expression of MCU and NCLX reduces autophagic activity under basal nutrient-rich conditions; (iii) decreased expression of MCU and NCLX modulates the expression of autophagy-related genes; (iv) the expression of NCLX is upregulated by nutrient depletion, which promotes autophagy; and (5) acute or chronic, genetic or pharmacological inhibition of NCLX suppresses starvation-induced autophagy.

How mitochondrial Ca^{2+} uptake through the MCU and efflux through NCLX can modulate overall cellular Ca^{2+} signaling, and consequently impact upon processes modulated by this ion, has been a target of extensive investigation in the literature. Along with the ER and plasma membrane, mitochondrial Ca^{2+} uptake is responsible for clearance of the ion from the cytosol during Ca^{2+} signaling events [13,15]. This was evidenced in our model by slower decay (increased half-life) after an ATP-induced Ca^{2+} peak in siMCU cells (**Figure 1K**). Conversely, inhibition of mitochondrial Ca^{2+} efflux can lead to accumulation of Ca^{2+} in mitochondria, and thus faster reduction in cytoplasmic Ca^{2+}, which was indeed observed with NCLX inhibition in this work and others [26,28]. Interestingly, siMCU and CGP did not change the Ca^{2+} peak after ATP stimulation, while siNCLX resulted in a significant reduction of peak intensity (**Figure 1J**). This NCLX KD effect is consistent with other observations in different cell types and forms of Ca^{2+} stimulation [25,28,37,38], associating reduced NCLX expression with an attenuation of cytoplasmic Ca^{2+} signals. Moreover, distinct effects of NCLX inhibition by siRNA-mediated KD and CGP were also observed in Ca^{2+} clearance rates, suggesting that chronic inhibition by KD may affect other Ca^{2+} pathways in the cell. In agreement, NCLX is in close proximity to the sarco/ER Ca^{2+}-ATPase (SERCA) [39], and participates in ER Ca^{2+} replenishment by modulating store-operated Ca^{2+} entry (SOCE) [28, 40-42]. Consequently, NCLX

KD can lead to defective Ca^{2+} handling by the ER [27], which may contribute to reduction in the Ca^{2+} peak after ATP stimulation, and slower clearance from the cytoplasm. Although the mechanisms are still being investigated, it is clear that NCLX activity has a strong impact on cellular Ca^{2+} signaling in a myriad of cell types and contexts.

How Ca^{2+} signals are involved in the regulation of autophagic activity has been studied [4,8], although several characteristics still remain to be investigated, including the role of mitochondrial Ca^{2+}, which we investigated here. We show that autophagy is particularly sensitive to chelation of intracellular Ca^{2+} in AML12 cells, as this significantly reduces autophagosome levels (**Figure 1A**). Indeed, autophagy machinery is known to be distinctly regulated by Ca^{2+}, and increases in cytosolic concentrations can both promote or inhibit autophagy at different regulatory checkpoints [43]. Considering Ca^{2+} uptake by mitochondria, previous studies have shown that Ca^{2+} transfer from the ER, through inositol trisphosphate receptor (IP_3R) and MCU tethering, suppresses basal autophagy by maintaining proper ATP synthesis, and therefore lowering AMPK activity [17,44]. While MCU and NCLX KD can affect oxidative phosphorylation in AML12 cells within a specific concentration range, under our conditions mitochondrial ATP production and AMPK activity were unchanged by MCU KD, since ATP-linked respiration (**Figure 3I**) and ULK1 phosphorylation at Ser555 (**Figure 3H**), were similar to controls. Indeed, we have previously shown that MCU KD in AML12 cells does not change basal respiration, but can limit maximal respiration induced by the presence of uncoupler [35]. In agreement, MEFs and mitochondria isolated from MCU KO mice do not present alterations in basal metabolic function [45]. Thus, the effects of reduced MCU expression on autophagy seen here are not related to changes in cellular bioenergetics.

Despite a lack of changes in ATP production, we did observe reduced autophagic flux after siMCU transfection by western blot analysis (**Figure 2A-D**), although there were no significant changes in autophagosome and autolysosome puncta in AML12-LC3 cells (**Figure 2G**). We speculate that alterations in cell mass/size might be leading to the different outcomes, since LC3 II levels are normalized by cell mass and puncta are relative to cell number. Alternatively, the external

LC3 expression system used as a probe may affect autophagosome formation in this context. Nonetheless, the fact that MCU KD also led to accumulation of polyubiquitinated proteins suggests lower autophagic activity (**Figure 2H and I**). Also, the finding that the cells have lower levels of ATG5–ATG12 conjugates, which are involved in LC3 I lipidation [3], agrees with decreased LC3 II levels (Fig. S2D). In line with this, MCU KD was shown to enhance palmitate-mediated autophagy impairment by increasing cytoplasmic Ca^{2+} concentrations in β cells [46], and specific MCU KD in the skeletal muscle of mice caused reduced autophagic flux *in vivo* [21]. Since Ca^{2+} uptake by mitochondria may affect cytosolic Ca^{2+} signaling and mitochondrial function, and both regulate autophagy, the consequences of decreased MCU activity are expected to vary depending on the cell type or conditions.

Our work also shows that reduction of NCLX activity led to markedly defective autophagy, in a manner dependent on cytosolic Ca^{2+} signaling. Prior studies observed the accumulation of damaged mitochondria in autophagosomes and higher LC3 II in NCLX KO cells, suggesting mitophagy induction due to impaired mitochondrial function [40,47], but overall autophagic activity was not investigated, and p62 was also accumulated, indicating that autophagic flux was reduced. The decreased accumulation of LC3 II in the presence of BafA1 (**Figure 2A and 5C**) and accumulation of LC3 I by CGP treatment (**Figure 6D and H**) indicates that NCLX inhibition is hampering the formation of autophagosomes under basal or stimulated conditions. In our model of chronic NCLX inhibition by siRNA, defective autophagosome formation under basal, nutrient-replete, conditions may be a consequence of reduction in the AMPK-ULK1 pathway. Interestingly, AMPKα1/α2 double KOs were shown to reduce ULK1 activity even under basal conditions [48], and ULK1 is known to regulate autophagy initiation. However, ULK1 activity is usually maintained at low levels under basal conditions by mTORC1 phosphorylation. Whether it has a role in NCLX-mediated autophagic regulation has yet to be investigated. Nonetheless, reduced phosphorylation of ULK1 at Ser555 in our work suggests that basal AMPK activity is decreased in siNCLX cells. In agreement, AMPK is known to be activated by intracellular Ca^{2+} through Ca^{2+}/calmodulin-dependent

kinase kinase-β (CaMKK-β) phosphorylation, even under basal conditions [49]. Hence, we hypothesize that reduced Ca^{2+} signals in siNCLX may suppress CaMKKI-β-AMPK activity, contributing to reduced autophagy. AMPK can also regulate the expression of autophagy-related genes by modulating TFEB and FOXO transcription factors [50-52]. In this context, our observation of reduced LC3 expression may be the main cause of impaired autophagy in siNCLX cells, as LC3 is essential for proper autophagosome formation [3]. Since TFEB can autoregulate its own expression [53], which was increased in siNCLX cells along with ATG5 and ATG12 mRNAs (Fig S2A), another transcription factor may be controlling LC3 mRNA levels; a candidate is FOXO3, shown to bind to the LC3 gene promoter region [54]. Moreover, FOXO transcription factors also regulate the expression of genes related to protein ubiquitination [55,56], which was reduced in siNCLX cells.

Autophagosome initiation and formation are directly regulated by Ca^{2+} signaling. For example, Ca^{2+}-release channels in the ER and lysosomes promote transient Ca^{2+} increases on the ER surface, which in turn are required for FIP200 recruitment to autophagosome initiation sites and, therefore, for autophagosome formation [57]. Since mitochondria are in close contact with the ER and lysosomes, including in autophagosome initiation sites [58-60], we hypothesize that mitochondrial Ca^{2+} efflux through NCLX participates in a similar mechanism. In agreement, CGP suppression of starvation-induced autophagy required the presence of Ca^{2+} (**Figure 6M**). Conversely, decreased autolysosome puncta were observed under nutrient-replete or starvation conditions, even when autophagosome steady-state levels were unchanged (**Figures 2G and 5I**), suggesting that later steps in autophagic machinery are concomitantly affected by NCLX activity, and demonstrating that the effects of this mitochondrial Ca^{2+} transporter on autophagy are widespread.

Indeed, NCLX activity was even more impactful under nutrient-starved conditions. Not only did NCLX inhibition suppress autophagy activation, but it also affected mTORC1 inhibition by amino acid and serum starvation. In this context, mTORC1 inhibition during starvation was shown to require cytosolic Ca^{2+}, since it was partially inhibited by treatment with BAPTA-AM [6]. Also, the fact that NCLX expression is increased under CR and starvation suggests that mitochondrial Ca^{2+} efflux has

a relevant function in nutrient-sensing pathways, which should further be explored. Overall, this data further strengthens the idea that mitochondrial calcium transporters are central sensors and regulators in metabolic processes.

Methods

Chemicals, reagents and antibodies

siRNA molecules, insulin-transferrin-selenium (ITS) solution, fetal bovine serum (FBS), DMEM/F-12, high glucose DMEM, HBSS, Ripa Buffer, Lipofectamine™ RNAiMAX and Lipofectamine™ 2000, Opti-MEM™, High-Capacity cDNA Reverse Transcription Kit, Platinum™ SYBR™ Green qPCR SuperMix-UDG, protease and phosphatase inhibitor cocktails, Pierce™ BCA Protein Assay Kit, Fura-2 AM, Ca^{2+} Green™-5N, and ProLong™ Diamond were purchased from Thermo Fisher Scientific (Waltham, MA, USA). CGP 37157 (1114) was purchased from Tocris/Bio-Techne (Bristol, UK). BAPTA-AM (A1076), Bafilomycin A1 (SML1661), and Rapamycin (R0395) were purchased from Sigma-Aldrich (St. Louis, MO, USA). Ionomycin (11932) was purchased from Cayman Chemical (Ann Arbor, MI, USA).

Primary antibody against β-actin (8226; 1:5,000) was purchased from Abcam (Cambridge, UK). Primary antibodies against LC3 A/B (12741; 1:1,000), LC3B (; 1:1,000), ATG7 (8558; 1:1,000), ATG12 (4180; 1:1,000), ULK1 (8054; 1:500), p-ULK S555 (5869, 1:500), p-ULK S757 (14202; 1:500), 4E-BP1 (9644; 1:1,000), p-4E-BP1 (2855; 1:1,000), MCU (14997; 1:1,000) and α-tubulin (3873; 1:10,000) were purchased from Cell Signaling Technology (Danvers, MA, USA). The primary antibody against total ubiquitin (sc-8017; 1:1,000) was purchased from Santa-Cruz Biotechnology (Dallas, TX, USA). NCLX antibody (orb317904; 1:500) was purchased from Biorbyt (Cambridge, UK).

Cell cultures

AML12 cells were purchased from ATCC® and cultivated in complete media (CM) consisting of DMEM/F-12 media supplemented with 10% FBS (v/v), 1% antibiotics (100 U/ml penicillin, 0.1 mg/ml streptomycin), and 1% ITS (Gibco™, 41400045). For retrovirus production, HEK 293FT cells (kindly donated by Prof. Alexandre-Bruni Cardoso) were cultivated in High Glucose DMEM media supplemented with 10% FBS (v/v) and 1% antibiotics. Cells were kept in a humidified incubator with a 5% CO_2 atmosphere, at 37°C, and trypsinized every 48-72 hours. The passage number was controlled up to 35. HBSS (Gibco™, 14175095) supplemented with 120 mg/L $CaCl_2$, 30 mg/L $MgCl_2$, and 50 mg/L $MgSO_4$ was used for serum and amino acid starvation experiments.

Small interference RNA (siRNA) transfection

AML12 cells were transfected with siRNAs targeting either NCLX (Ambion®, ID s100747) or MCU (Ambion®, ID s103465) mRNAs or with a Negative Control (NC) sequence (Ambion®, 4390843) at a final concentration of 20 nM. Transfections were performed using the Lipofectamine™ RNAiMAX (Invitrogen™, 13778030) reagent through a reverse transfection protocol. Briefly, Lipofectamine™ and siRNAs were mixed in Opti-MEM™ media and incubated for 5-10 minutes at room temperature. Cells were suspended in transfection media (DMEM/F-12, 10% FBS, 1% ITS, without antibiotics) and added to the plate well on top of the Lipofectamine™-siRNA complexes. The transfection media was replaced by CM 24 hours later, and experiments were performed 48-72 hours after transfection. Importantly, for experiments performed at 72 hours, the cells were trypsinized and re-seeded in new culture plates 24 hours earlier.

RT-qPCR

RNA was isolated from cells using Trizol® reagent following the manufacturer's instructions. The concentration of isolated RNA was quantified using a NanoDrop® spectrophotometer and 1-2 µg was used for cDNA synthesis with a High-Capacity cDNA Reverse Transcription Kit (Applied

Biosystems™, 4368814). qPCR reactions were conducted using a 7500 Real-Time PCR System (Applied Biosystems™) with Platinum™ SYBR™ Green qPCR SuperMix-UDG (Invitrogen™, 11733046), 10 ng of cDNA, and the specific primers described in Supplementary Table 1. The Ct values were analyzed through the $2^{(-\Delta\Delta Ct)}$ method and the housekeeping gene or combination of genes were chosen by testing the expression of *Hmbs*, *B2m* and *Actb* in each experimental group. The compared stability value was calculated using NormFinder Software [61]. The mean Ct value between *Hmbs* and *B2m* expression was used as housekeeping for experiments containing siRNA-mediated knockdown groups. For experiments containing HBSS and rapamycin time curve treatments, a Ct value of *B2m* was used.

Mitochondrial Ca^{2+} uptake in permeabilized cells

To evaluate the rate of Ca^{2+} uptake by mitochondria we used a digitonin-permeabilization protocol, as previously described [31,63]. Initially, optimal digitonin concentrations were titrated for each experimental group, as follows: cells were trypsinized, washed once with experimental buffer (125 mM sucrose, 65 mM KCl, 2 mM $MgCl_2$, 2 mM KH_2PO_4, 0.1 mg/mL fatty acid-free BSA, 10 mM HEPES, pH 7.2 adjusted with KOH) containing 1 mM EGTA; cells were then resuspended in 2 mL of experimental buffer. Cell number was determined and 2×10^6 cells per group were added to a high-resolution Oxygraph-2k (O2k) respirometer (Oroboros Instruments, Innsbruck, Austria) chamber in 2 mL of experimental buffer containing 1 mM EGTA, 2 mM succinate, 1 µM rotenone, and 1 mM ADP. Under these conditions, only cells in which the outer membrane was permeabilized can respire, since succinate is not membrane-permeable. Titration was made through sequential 1 µL additions of 0.5% digitonin (w/v), and the optimal concentration was that which presented the highest oxygen consumption rate.

For Ca^{2+} uptake experiments, 2×10^6 cells were added to a cuvette in 2 mL of experimental buffer containing 2 mM pyruvate, 2 mM malate, 10 µM EGTA, 5 µL of 0.5% digitonin, and 75 nM Ca^{2+} Green™-5N. The cuvette was placed in a F2500 Hitachi Fluorimeter at 37ºC with continuous

stirring and Ca^{2+} Green™-5N fluorescence was measured at λex = 506 nm and λem = 532 nm. Sequential additions of 10 µM $CaCl_2$ boluses were made and a decrease in extramitochondrial Ca^{2+} concentration due to mitochondrial uptake was recorded between each addition. After mitochondria underwent mitochondrial permeability transition, marked by a significant increase in extramitochondrial Ca^{2+} concentrations due to loss of inner membrane impermeability, two sequential additions of 5 µM $CaCl_2$, followed by the addition of 1 mM EGTA (for minimum fluorescence) and 10 mM $CaCl_2$ (for maximum fluorescence) were made for calibration purposes. Fluorescence values were converted to Ca^{2+} concentration using the equation $[Ca^{2+}] = Kd \cdot (F - F_{min})/(F_{max} - F)$, where the Kd value for Ca^{2+} Green™-5N was determined by iteration.

Cytosolic Ca^{2+} measurements

Initially, cells were incubated with a mix of 5 µM Fura-2 AM (Invitrogen™, F1221) and 0.025% Pluronic® F-127 (diluted in CM) for 10 minutes at 37°C for Fura-2 loading. Next, cells were trypsinized, centrifuged, washed once with 1X PBS, and resuspended in HBSS (5.5 mM D-Glucose, 120 mg/L $CaCl_2$, 30 mg/L $MgCl_2$, 50 mg/L $MgSO_4$, 60 mg/L KH_2PO_4, 48 mg/L Na_2HPO_4, 400 mg/L KCl, 8 g/L NaCl, 350 mg/L $NaHCO_3$, 5 mM HEPES). The cell number was determined and 1×10^6 cells were added to a cuvette to a final volume of 2 mL. Importantly, for experiments using pharmacological inhibition, DMSO (equal volume, as a control) or CGP 37157 were added to the cuvette before fluorescence measurement started. The cuvette was placed in a F4500 Hitachi Fluorimeter at 37ºC with continuous stirring and Fura-2 fluorescence was detected at λex = 340/380 nm and λem = 505 nm. The addition of 100 µM ATP was used to stimulate an increase in cytosolic Ca^{2+} levels, which were analyzed as the ratio between fluorescence emission at 340 nm and 380 nm excitation (340/380) relative to the basal ratio (R_1/R_0). Peak height, area under the curve (AUC) and half-life after the peak were calculated using GraphPad Prism 7 software.

Mitochondrial Ca^{2+} efflux in intact cells

To estimate mitochondrial Ca^{2+} efflux rates in live cells, we measured intramitochondrial free Ca^{2+} levels by transfecting AML12 cells with the CMV-mito-GEM-GECO1 plasmid (Addgene, 32461; gifted from Robert Campbell) [36]. Briefly, cells were seeded in a glass bottom culture dish (Greiner Bio-One, 627870) and, 24 hours later, the media was replaced with transfection media (DMEM/F-12, 10% FBS, 1% ITS, without antibiotics). The plasmid was transfected using Lipofectamine™ 2000 Transfection Reagent (Invitrogen™, 11668019) at a 1:1 µg DNA to µL Lipofectamine™ ratio, following the manufacturer's protocol. The media was replaced for CM 24 hours after transfection and the cells were imaged after an additional 24 hours. For imaging, the media was replaced for HBSS (5.5 mM D-glucose, 120 mg/L $CaCl_2$, 30 mg/L $MgCl_2$, 50 mg/L $MgSO_4$, 60 mg/L KH_2PO_4, 48 mg/L Na_2HPO_4, 400 mg/L KCl, 8 g/L NaCl, 350 mg/L $NaHCO_3$, 5 mM HEPES) containing either DMSO or CGP 37157 and fluorescence was acquired in a Zeiss LSM 780-NLO confocal microscope using a 405 nm diode laser and a C-Apochromat" 63x/1.20 DIC objective, in an environment kept at 37°C, with 5% CO_2 atmosphere. During acquisition, cells were imaged every 4 seconds for at least 15 minutes. 100 µM ATP was added to stimulate intramitochondrial Ca^{2+} increases and 10 µM ionomycin was used to compare the maximum fluorescence ratio between groups. Analysis was performed using the Fiji ImageJ software and results are shown as the ratio between emissions at 455 nm and 511 nm relative to the basal ratio (R_1/R_0). Mitochondrial efflux rates were calculated as the slope after the ATP-stimulated Ca^{2+} peak, using the GraphPad Prism 7 software.

Western blots

Cells were washed with 1X ice-cold PBS and lysed in RIPA buffer containing protease and phosphate inhibitor cocktail (Thermo Scientific™, 78443). Cell lysates were sonicated using a probe sonicator and protein concentration was quantified using the Pierce™ BCA Protein Assay Kit (Thermo Scientific™, 23227). Samples were prepared in 1X Laemmli buffer (2% SDS, 10% glycerol,

0.062 M Tris pH 6.8, 0.002% bromophenol blue, 5% 2-mercaptoethanol), loaded onto SDS-PAGE for gel electrophoresis separation, and transferred overnight to PVDF membranes using a wet transfer system. Membranes were blocked in TTBS (20 mM Tris pH 7.5, 150 mM NaCl and 0.1% Tween 20) containing 3-5% BSA (w/v) before overnight incubation with primary antibodies at 4°C. After washing with TTBS, membranes were incubated with fluorescent IRDye® secondary antibodies (1:15,000) for 1 hour at room temperature. Fluorescence was detected using the ChemiDoc™ Imaging System (Bio-Rad) and band densitometry was quantified using Fiji ImageJ software.

mCherry-EGFP-LC3B expression, imaging, and analysis

To evaluate autophagic activity, we generated an AML12 cell line stably expressing mCherry-EGFP-tagged LC3B protein. Retroviruses were produced by transfecting HEK 293FT cells with a pBABE-puro-mCherry-EGFP-LC3B plasmid (Addgene, 22418; gifted by Jayanta Debnath) [33] and a PCL-Eco packaging plasmid (Addgene, 12371; gifted by Inder Verma) [63]. 48-72 hours after transfection, the media from the HEK 293FT cells was used to transduce AML12 cells through multiple rounds of infection. 24 hours after the last infection, cells were kept in CM containing 10 µg/mL puromycin for five days. After selection, cells were cultivated in CM supplemented with 1 µg/mL puromycin, which was removed from the media during experiments.

For experiments, AML12-LC3 cells were transfected with specific siRNAs using the same protocol (described in the "*Small interference RNA (siRNA) transfection"* section). 48 hours after transfection, cells were trypsinized, seeded on poly-D-lysine-coated 12 mm coverslips (Thorlabs, CG15NH) and incubated for additional 24 hours before treatments. After treatments, media was removed and cells were fixed in 4% paraformaldehyde for 15 minutes at room temperature. Coverslips were washed once with 1X PBS containing 0.1 M Glycine, washed two times with 1X PBS and incubated with DAPI (0.1 µg/mL) for 10 minutes at room temperature. Finally, coverslips were washed three times with 1X PBS and mounted onto glass slides using ProLong™ Diamond Antifade Mountant (Invitrogen™, P36965). Images were acquired using a Leica DMi8 microscope

with an HC PL APO CS2 63x/1.40 OIL UV objective. At least 100 cells per group were imaged and each channel was acquired through 2 µm on the Z-axis dimension (total of 6 steps). Images were processed using the Leica 3D BlindDeblur deconvolution tool and $mCherry^+/GFP^+$ (autophagosome), $mCherry^+/GFP^-$ (autolysosome), and cell number (DAPI) were quantified using Fiji ImageJ software.

Proteasome activity

72 hours after siRNA transfection, cells were trypsinized, washed once with 1X cold PBS and resuspended in experimental buffer (5 mM $MgCl_2$, 50 mM Tris, pH 7.5). Next, cells were lysed using an insulin syringe and centrifuged for 10 min at 10,000 × g, at 4°C for debris separation. Protein concentration was quantified using the Pierce™ BCA Protein Assay Kit (Thermo Scientific™, 23227) and 30 µg of protein (in 100 µL of experimental buffer) was added to each well for the assay. To measure proteasome (chymotrypsin-like) activity, cell extracts were incubated with 250 µM fluorogenic peptide Suc-LLVY-AMC and the increase in AMC fluorescence was monitored for 10 minutes at 37°C, using a Flex Station 3 (Molecular Devices) microplate fluorescence spectrophotometer (λex = 341 nm, λem = 441 nm). The slope of fluorescence increase over time was quantified using GraphPad Prism 7 software and proteasome activity was validated by replicating the assay in the presence of 50 µM Bortezomib (proteasome inhibitor).

ATP-linked respiration

Mitochondrial oxygen consumption linked to ATP production was measured using a Seahorse Extracellular Flux Analyzer (Agilent Technologies, Santa Clara, CA, EUA) as described previously [35]. Briefly, 3×10^4 cells per well were seeded in CM 24 hours before analysis. On the next day, cells were washed three times with DMEM/F-12 media supplemented with 1% antibiotics and 5 mM HEPES (without bicarbonate and FBS) and were incubated in the same media for 1 hour, at 37°C in a normal atmosphere. Oxygen consumption rates were measured under basal conditions and after the injection of 1 µM oligomycin to calculate ATP-linked respiration. After the experiment, cells were

lysed in Ripa Buffer and total protein was quantified using the Pierce™ BCA Protein Assay Kit (Thermo Scientific™, 23227) for data normalization.

Caloric restriction diet and mitochondrial isolation

Eight-week-old male Swiss mice were divided into *ad libitum* (AL) and caloric restriction (CR), eating 40% less calories than AL animals with micronutrient supplementation for 4 weeks [64]. The diet was adjusted weekly according to the AL animals' food intake. Both chow diets were prepared by Rhoster® (Campinas, SP, Brazil). All animal experiments were approved by the animal ethical committee and followed National Institutes of Health guidelines for animal welfare.

After the diet period, mitochondria was isolated from the liver of mice as described previously [63]. Briefly, the livers were minced, washed repeatedly with ice-cold PBS and suspended in isolation buffer (250 mM Sucrose, 10 mM HEPES, 1 mM EGTA, 1 mM EDTA, 1 mg/ml BSA fatty acid-free). Tissues were homogenized using a Potter-Elvehjem tissue grinder, and mitochondria were isolated by differential centrifugation.

Statistical analysis

Statistical analysis was performed using GraphPad Prism 7 software. At least three independent biological replicates were made for each experiment, and these are represented by individual dots in the graphs. Dots of the same color/pattern in different groups represent paired biological replicates. Data comparing two groups were analyzed with Student's t-test. Data comparing three different groups (e.g., siNC, siNCLX and siMCU) were analyzed with one-way randomized blocks ANOVA followed by Bonferroni's multiple comparison test. Data comparing two factors (e.g., siRNA and Bafilomycin A1) were analyzed with two-way randomized blocks ANOVA followed by either Bonferroni's (when comparing only column effects) or Tukey's (when comparting effects regardless of rows or columns) multiple comparisons test. Results are shown as means ± SD and * = $p < 0.05$, ** = $p < 0.01$, *** = $p < 0.001$, **** = $p < 0.0001$, ns = not significant.

Acknowledgements

This work was supported mainly by the *Fundação de Amparo à Pesquisa do Estado de São Paulo* (FAPESP) under grant numbers 13/07937-8, 20/06970-5, as well as the *Conselho Nacional de Desenvolvimento Científico e Tecnológico* (CNPq) and *Coordenação de Aperfeiçoamento de Pessoal de Nível Superior* (CAPES) line 001. Authors were supported by FAPESP fellowships #2019/18402-4, #2019/05226-3, #2021/02481-2, #2017/14713-0. We acknowledge Silvânia M. P. Neves and her animal facility crew for exceptional expert animal care; Natália Soares Ferreira and Mario Costa Cruz from the *Centro de Facilidades de Apoio à Pesquisa* (CEFAP) for excellent technical assistance in the Confocal experiments; Camille C. Caldeira da Silva and Sirlei Mendes de Oliveira for the remarkable technical support. We also acknowledge Dr. Sergio Menezes-Filho for initial animal experiments and Prof Alexandre Bruni-Cardoso for reagent donation.

Disclosure statement

The authors declare that they have no conflicts of interest with the contents of this article.

References

[1] Mizushima N, Komatsu M. Autophagy: renovation of cells and tissues. Cell. 2011 Nov 11; 147(4):728-41. PMID: 22078875.

[2] Lahiri V, Hawkins WD, Klionsky DJ. Watch what you (self-) eat: autophagic mechanisms that modulate metabolism. Cell Metab. 2019 Apr 2; 29(4):803-826. PMID: 30943392.

[3] Chen Y, Klionsky DJ. The regulation of autophagy - unanswered questions. J Cell Sci. 2011 Jan 15; 124(Pt 2):161-70. PMID: 21187343.

[4] Filippi-Chiela EC, Viegas MS, Thomé MP, et al. Modulation of autophagy by calcium signalosome in human disease. Mol Pharmacol. 2016 Sep; 90(3):371-84. PMID: 27436127.

[5] Berridge MJ, Lipp P, Bootman MD. The versatility and universality of calcium signalling. Nat Rev Mol Cell Biol. 2000 Oct;1(1):11-21. doi: 10.1038/35036035. PMID: 11413485.

[6] Ghislat G, Patron M, Rizzuto R, Knecht E. Withdrawal of essential amino acids increases autophagy by a pathway involving Ca^{2+}/calmodulin-dependent kinase kinase-β (CaMKK-β). J Biol Chem. 2012 Nov 9; 287(46):38625-36. PMID: 23027865.

[7] Zhou X, Clister TL, Lowry PR, et al. Dynamic visualization of mTORC1 activity in living cells. Cell Rep. 2015 Mar 17; 10(10):1767-1777. PMID: 25772363.

[8] Zhang R, Kang R, Klionsky DJ, Tang D. Ion channels and transporters in autophagy. Autophagy. 2022 Jan; 18(1):4-23. PMID: 33657975.

[9] Medina DL, Di Paola S, Peluso I, et al. Lysosomal calcium signalling regulates autophagy through calcineurin and TFEB. Nat Cell Biol. 2015 Mar; 17(3):288-99. PMID: 25720963.

[10] Giorgi C, Marchi S, Pinton P. The machineries, regulation and cellular functions of mitochondrial calcium. Nat Rev Mol Cell Biol. 2018 Nov; 19(11):713-730. Erratum in: Nat Rev Mol Cell Biol. 2018 Sep 24; PMID: 30143745.

[11] Rizzuto R, De Stefani D, Raffaello A, Mammucari C. Mitochondria as sensors and regulators of calcium signalling. Nat Rev Mol Cell Biol. 2012 Sep; 13(9):566-78. PMID: 22850819.

[12] Boitier E, Rea R, Duchen MR. Mitochondria exert a negative feedback on the propagation of intracellular Ca2+ waves in rat cortical astrocytes. J Cell Biol. 1999 May 17; 145(4):795-808. PMID: 10330407.

[13] Drago I, De Stefani D, Rizzuto R, Pozzan T. Mitochondrial Ca^{2+} uptake contributes to buffering cytoplasmic Ca^{2+} peaks in cardiomyocytes. Proc Natl Acad Sci U S A. 2012 Aug 7; 109(32):12986-91. PMID: 22822213.

[14] Kaftan EJ, Xu T, Abercrombie RF, Hille B. Mitochondria shape hormonally induced cytoplasmic calcium oscillations and modulate exocytosis. J Biol Chem. 2000 Aug 18; 275(33):25465-70. PMID: 10835418.

[15] De Stefani D, Rizzuto R, Pozzan T. Enjoy the Trip: Calcium in mitochondria back and forth. Annu Rev Biochem. 2016 Jun 2; 85:161-92. PMID: 27145841.

[16] De Stefani D, Raffaello A, Teardo E, et al. A forty-kilodalton protein of the inner membrane is the mitochondrial calcium uniporter. Nature. 2011 Jun 19; 476(7360):336-40. PMID: 21685888.

[17] Cárdenas C, Miller RA, Smith I, et al. Essential regulation of cell bioenergetics by constitutive InsP3 receptor Ca^{2+} transfer to mitochondria. Cell. 2010 Jul 23; 142(2):270-83. PMID: 20655468.

[18] Yu Z, Chen R, Li M, et al. Mitochondrial calcium uniporter inhibition provides cardioprotection in pressure overload-induced heart failure through autophagy enhancement. Int J Cardiol. 2018 Nov 15; 271:161-168. PMID: 29803339.

[19] Granatiero V, Giorgio V, Calì T, et al. Reduced mitochondrial Ca^{2+} transients stimulate autophagy in human fibroblasts carrying the 13514A>G mutation of the ND5 subunit of NADH dehydrogenase. Cell Death Differ. 2016 Feb; 23(2):231-41. PMID: 26206091.

[20] MacVicar TD, Mannack LV, Lees RM, Lane JD. Targeted siRNA Screens identify ER-to-mitochondrial calcium exchange in autophagy and mitophagy responses in RPE1 cells. Int J Mol Sci. 2015 Jun 11; 16(6):13356-80. PMID: 26110381.

[21] Gherardi G, Di Marco G, Rizzuto R, Mammucari C. Crosstalk between mitochondrial Ca^{2+} uptake and autophagy in skeletal muscle. Oxid Med Cell Longev. 2019 Sep 8; 2019:1845321. PMID: 31583037

[22] Yu S, Zheng S, Leng J, et al. Inhibition of mitochondrial calcium uniporter protects neurocytes from ischemia/reperfusion injury via the inhibition of excessive mitophagy. Neurosci Lett. 2016 Aug 15; 628:24-9. PMID: 27288019.

[23] Patron M, Tarasenko D, Nolte H, et al. Regulation of mitochondrial proteostasis by the proton gradient. EMBO J. 2022 Aug 16; 41(16):e110476. PMID: 35912435.

[24] Palty R, Silverman WF, Hershfinkel M, et al. NCLX is an essential component of mitochondrial Na^+/Ca^{2+} exchange. Proc Natl Acad Sci U S A. 2010 Jan 5; 107(1):436-41. PMID: 20018762.

[25] Nita II, Hershfinkel M, Fishman D, et al. The mitochondrial Na^+/Ca^{2+} exchanger upregulates glucose dependent Ca^{2+} signalling linked to insulin secretion. PLoS One. 2012; 7(10):e46649. PMID: 23056385.

[26] Cabral-Costa JV, Vicente-Gutiérrez C, Agulla J, et al. Mitochondrial sodium/calcium exchanger NCLX regulates glycolysis in astrocytes, impacting on cognitive performance. J Neurochem. 2022 Dec 23. Epub ahead of print. PMID: 36563047.

[27] Takeuchi A, Kim B, Matsuoka S. The mitochondrial Na^+-Ca^{2+} exchanger, NCLX, regulates automaticity of HL-1 cardiomyocytes. Sci Rep. 2013 Sep 26; 3:2766. PMID: 24067497.

[28] Parnis J, Montana V, Delgado-Martinez I, et al. Mitochondrial exchanger NCLX plays a major role in the intracellular Ca^{2+} signaling, gliotransmission, and proliferation of astrocytes. J Neurosci. 2013 Apr 24; 33(17):7206-19. PMID: 23616530.

[29] Garbincius JF, Elrod JW. Mitochondrial calcium exchange in physiology and disease. Physiol Rev. 2022 Apr 1; 102(2):893-992. PMID: 34698550.

[30] Wu JC, Merlino G, Fausto N. Establishment and characterization of differentiated, nontransformed hepatocyte cell lines derived from mice transgenic for transforming growth factor alpha. Proc Natl Acad Sci U S A. 1994 Jan 18; 91(2):674-8. PMID: 7904757.

[31] Fiskum G, Craig SW, Decker GL, Lehninger AL. The cytoskeleton of digitonin-treated rat hepatocytes. Proc Natl Acad Sci U S A. 1980 Jun; 77(6):3430-4. PMID: 6997878.

[32] Yoshii SR, Mizushima N. Monitoring and measuring autophagy. Int J Mol Sci. 2017 Aug 28; 18(9):1865. PMID: 28846632.

[33] N'Diaye EN, Kajihara KK, Hsieh I, et al. PLIC proteins or ubiquilins regulate autophagy-dependent cell survival during nutrient starvation. EMBO Rep. 2009 Feb; 10(2):173-9. PMID: 19148225.

[34] Zachari M, Ganley IG. The mammalian ULK1 complex and autophagy initiation. Essays Biochem. 2017 Dec 12; 61(6):585-596. PMID: 29233870.

[35] Vilas-Boas EA, Cabral-Costa JV, Ramos VM, et al. Goldilocks calcium concentrations and the regulation of oxidative phosphorylation: Too much, too little, or just right. J Biol Chem. 2023 Jan 13; 299(3):102904. Epub ahead of print. PMID: 36642177.

[36] Zhao Y, Araki S, Wu J, et al. An expanded palette of genetically encoded Ca^{2+} indicators. Science. 2011 Sep 30; 333(6051):1888-91. PMID: 21903779.

[37] Stavsky A, Stoler O, Kostic M, et al. Aberrant activity of mitochondrial NCLX is linked to impaired synaptic transmission and is associated with mental retardation. Commun Biol. 2021 Jun 2; 4(1):666. Erratum in: Commun Biol. 2021 Jun 14;4(1):755. PMID: 34079053.

[38] Kim B, Takeuchi A, Koga O, et al. Pivotal role of mitochondrial Na^+-Ca^{2+} exchange in antigen receptor mediated Ca^{2+} signalling in DT40 and A20 B lymphocytes. J Physiol. 2012 Feb 1;590(3):459-74. PMID: 22155933.

[39] Takeuchi A, Matsuoka S. Spatial and functional crosstalk between the mitochondrial Na^+-Ca^{2+} exchanger NCLX and the sarcoplasmic reticulum Ca^{2+} pump SERCA in cardiomyocytes. Int J Mol Sci. 2022 Jul 19; 23(14):7948. PMID: 35887296.

[40] Emrich SM, Yoast RE, Fike AJ, et al. The mitochondrial sodium/calcium exchanger NCLX (Slc8b1) in B lymphocytes. Cell Calcium. 2022 Dec; 108:102667. PMID: 36308855.

[41] Malli R, Graier WF. The role of mitochondria in the activation/maintenance of SOCE: the contribution of mitochondrial Ca^{2+} uptake, mitochondrial motility, and location to store-operated ca^{2+} entry. Adv Exp Med Biol. 2017; 993:297-319. PMID: 28900921.

[42] Ben-Kasus Nissim T, Zhang X, Elazar A, et al. Mitochondria control store-operated Ca^{2+} entry through Na^+ and redox signals. EMBO J. 2017 Mar 15; 36(6):797-815. PMID: 28219928.

[43] Decuypere JP, Bultynck G, Parys JB. A dual role for Ca^{2+} in autophagy regulation. Cell Calcium. 2011 Sep; 50(3):242-50. PMID: 21571367.

[44] Mallilankaraman K, Cárdenas C, Doonan PJ, et al. MCUR1 is an essential component of mitochondrial Ca^{2+} uptake that regulates cellular metabolism. Nat Cell Biol. 2012 Dec; 14(12):1336-43. Erratum in: Nat Cell Biol. 2013 Jan;15(1):123. Erratum in: Nat Cell Biol. 2015 Jul;17(7):953. PMID: 23178883.

[45] Pan X, Liu J, Nguyen T, et al. The physiological role of mitochondrial calcium revealed by mice lacking the mitochondrial calcium uniporter. Nat Cell Biol. 2013 Dec; 15(12):1464-72. PMID: 24212091.

[46] Ly LD, Ly DD, Nguyen NT, et al. Mitochondrial Ca^{2+} uptake relieves palmitate-induced cytosolic Ca^{2+} overload in MIN6 cells. Mol Cells. 2020 Jan 31; 43(1):66-75. PMID: 31931552.

[47] Pathak T, Gueguinou M, Walter V, et al. Dichotomous role of the human mitochondrial $Na^+/Ca^{2+}/Li^+$ exchanger NCLX in colorectal cancer growth and metastasis. Elife. 2020 Sep 11; 9:e59686. Erratum in: Elife. 2023 Feb 09;12: PMID: 32914752.

[48] Kim J, Kundu M, Viollet B, Guan KL. AMPK and mTOR regulate autophagy through direct phosphorylation of Ulk1. Nat Cell Biol. 2011 Feb; 13(2):132-41. PMID: 21258367.

[49] Høyer-Hansen M, Bastholm L, Szyniarowski P, et al. Control of macroautophagy by calcium, calmodulin-dependent kinase kinase-beta, and Bcl-2. Mol Cell. 2007 Jan 26; 25(2):193-205. PMID: 17244528.

[50] Li J, Sun Q, Qiu X, et al. Downregulation of AMPK dependent FOXO3 and TFEB involves in the inhibition of autophagy in diabetic cataract. Curr Eye Res. 2022 Apr; 47(4):555-564. PMID: 34872443.

[51] Wang S, Li H, Yuan M, et al. Role of AMPK in autophagy. Front Physiol. 2022 Nov 25; 13:1015500. PMID: 36505072.

[52] Li XN, Song J, Zhang L, et al. Activation of the AMPK-FOXO3 pathway reduces fatty acid-induced increase in intracellular reactive oxygen species by upregulating thioredoxin. Diabetes. 2009 Oct; 58(10):2246-57. PMID: 19592618.

[53] Settembre C, Fraldi A, Medina DL, Ballabio A. Signals from the lysosome: a control centre for cellular clearance and energy metabolism. Nat Rev Mol Cell Biol. 2013 May; 14(5):283-96. PMID: 23609508.

[54] Mammucari C, Milan G, Romanello V, et al. FoxO3 controls autophagy in skeletal muscle in vivo. Cell Metab. 2007 Dec; 6(6):458-71. PMID: 18054315.

[55] Lapierre LR, Kumsta C, Sandri M, et al. Transcriptional and epigenetic regulation of autophagy in aging. Autophagy. 2015; 11(6):867-80. PMID: 25836756.

[56] Milan G, Romanello V, Pescatore F, et al. Regulation of autophagy and the ubiquitin-proteasome system by the FoxO transcriptional network during muscle atrophy. Nat Commun. 2015 Apr 10; 6:6670. PMID: 25858807.

[57] Zheng Q, Chen Y, Chen D, et al. Calcium transients on the ER surface trigger liquid-liquid phase separation of FIP200 to specify autophagosome initiation sites. Cell. 2022 Oct 27; 185(22):4082-4098.e22. PMID: 36198318.

[58] Rizzuto R, Pinton P, Carrington W, et al. Close contacts with the endoplasmic reticulum as determinants of mitochondrial Ca^{2+} responses. Science. 1998 Jun 12; 280(5370):1763-6. PMID: 9624056.

[59] Peng W, Wong YC, Krainc D. Mitochondria-lysosome contacts regulate mitochondrial Ca^{2+} dynamics via lysosomal TRPML1. Proc Natl Acad Sci U S A. 2020 Aug 11;117(32):19266-19275. PMID: 32703809.

[60] Hamasaki M, Furuta N, Matsuda A, et al. Autophagosomes form at ER-mitochondria contact sites. Nature. 2013 Mar 21; 495(7441):389-93. PMID: 23455425.

[61] Andersen CL, Jensen JL, Ørntoft TF. Normalization of real-time quantitative reverse transcription-PCR data: a model-based variance estimation approach to identify genes suited for normalization, applied to bladder and colon cancer data sets. Cancer Res. 2004 Aug 1; 64(15):5245-50. PMID: 15289330.

[62] Serna JDC, Ramos VM, Cabral-Costa JV, et al. Measuring mitochondrial Ca^{2+} efflux in isolated mitochondria and permeabilized cells. Bioenergetics Communications. 2022 Jul 28; 2022:1-7.

[63] Naviaux RK, Costanzi E, Haas M, Verma IM. The pCL vector system: rapid production of helper-free, high-titer, recombinant retroviruses. J Virol. 1996 Aug; 70(8):5701-5. PMID: 8764092.

[64] Menezes-Filho SL, Amigo I, Prado FM, et al. Caloric restriction protects livers from ischemia/reperfusion damage by preventing Ca^{2+}-induced mitochondrial permeability transition. Free Radic Biol Med. 2017 Sep; 110:219-227. PMID: 28642067.

Figures legends

Figure 1. Knockdown of mitochondrial Ca^{2+} transporters shapes mitochondrial and cytosolic Ca^{2+} handling. (**A**) LC3 II western blot analysis of AML12 cells incubated with 50 µM BAPTA-AM in complete media (CM) for 3 hours (n = 4). (**B-E**) AML12 cells transfected with NCLX (siNCLX), MCU (siMCU) or negative control (siNC) siRNAs were analyzed by RT-qPCR for NCLX and MCU mRNA, 48 and 72 hours after transfection (n = 5-6). Data were analyzed by two-tailed paired t test. (**F, G**) Mitochondrial Ca^{2+} retention capacity and (**H**) Ca^{2+} uptake rate measured in digitonin-permeabilized AML12 cells, 72 hours after transfection. Arrows in F indicate 10 µM Ca^{2+} bolus additions (n = 3-4). The inset in H shows representative magnified uptake rates after the first Ca^{2+} bolus, used for calculations. Data were analyzed by one-way ANOVA, followed by Bonferroni's multiple comparison test. (**I**) Representative traces of cytosolic Ca^{2+} measurements using Fura-2 AM and stimulation with 100 µM ATP. (**J**) Ca^{2+} peak quantification and (**K**) half-life of one phase decay after the peak from experiments such as depicted in I (n = 5). Data were analyzed by one-way RM ANOVA followed by Bonferroni's multiple comparison test. Bar graphs show means ± SD. Dots in each group represent biological replicates and dots of equal color indicate paired replicates. * = $p < 0.05$, ** = $p < 0.01$, *** = $p < 0.001$, **** = $p < 0.0001$, ns = not significant.

Figure 2. NCLX and MCU knockdown impair basal autophagy. AML12 cells transfected with NCLX (siNCLX), MCU (siMCU) or negative control (siNC) siRNAs were analyzed by (**A-C**) western blot for levels of LC3 I and LC3 II proteins 72 hours after transfection, under complete media (CM) conditions and in the absence (Basal) or presence of 100 nM Bafilomycin A1 (+BafA1) for 1 hour (n = 6). Data were analyzed by two-way randomized blocks ANOVA followed by Bonferroni's multiple comparisons test. (**D**) LC3 II net flux calculated as the difference in LC3 II levels between samples treated with Bafilomycin A1 minus untreated samples (n = 6). Data were analyzed by one-way RM ANOVA followed by Bonferroni's multiple comparison test. (**E**) RT-qPCR for LC3A and LC3B mRNA, 48 and 72 hours after transfection (n = 5-6). Data were analyzed by two-tailed paired t tests. (**F,G**) Representative images and quantification of autophagosomes ($mCherry^{+}/GFP^{+}$; yellow

puncta) and autolysosomes (mCherry^{+}/GFP^{-}; red puncta) per cell in AML12 cells stably expressing the mCherry-EGFP-LC3B probe, 72 hours after siRNA transfection (n = 4). Data were analyzed by two-way randomized blocks ANOVA followed by Bonferroni's multiple comparisons test. (**F**) Western blot analysis for total polyubiquitinated proteins (Ub) in AML12 cells 72 hours after siRNA transfection in complete media (CM) under basal conditions (n = 6) or (**H**) after treatment with 100 nM Bafilomycin A1 (+BafA1, **I**) for 1 hour (n = 4). Coomassie staining of the membrane was used as a loading control. Data were analyzed by one-way RM ANOVA followed by Bonferroni's multiple comparison test. Bar graphs show mean ± SD. Dots in each group represent biological replicates and dots of equal color indicate paired replicates. * = $p < 0.05$, ** = $p < 0.01$, *** = $p < 0.001$, ns = not significant.

Figure 3. NCLX KD suppresses ULK1 phosphorylation by AMPK. Western blot analysis of AML12 cells 72 hours after transfection with NCLX (siNCLX), MCU (siMCU), or negative control (siNC) siRNAs and quantification of (**A**) total ULK1 protein levels, (**B**) ULK1 phosphorylation at Serine 757 (S757), (**C**) p-ULK1 (S757) relative to total ULK1, (**D**) total 4E-BP1 protein levels, (**E**) 4E-BP1 phosphorylation at Threonine 37/46, (**F**) p-4E-BP1 relative to total 4E-BP1, (**G**) ULK1 phosphorylation at Serine 555 (S555) and (**H**) p-ULK1 (S555) relative to total ULK1 (n = 5). (**I**) Oxygen consumption rates (OCR) linked to ATP synthesis (oligomycin-sensitive respiration) of transfected AML12 cells in complete media (CM) (n = 4). Data were analyzed by one-way RM ANOVA followed by Bonferroni's multiple comparison test. Bar graphs show mean ± SD, dots in each group represent biological replicates and dots of equal color indicate paired replicates. * = $p < 0.05$, ** = $p < 0.01$, *** = $p < 0.001$, ns = not significant.

Figure 4. NCLX expression is increased by pro-autophagic stimuli. RT-qPCR for (**A**) MCU and (**B**) NCLX mRNA in AML12 cells treated with either complete media (CM), HBSS or 200 nM rapamycin for 3, 6, and 24 hours (n = 4). Data were analyzed by two-way randomized blocks ANOVA followed by Bonferroni's multiple comparisons test. (**C**) Western blot analysis of NCLX protein levels in mitochondria isolated from the livers of Swiss mice after 4 months of *ad libitum* (AL) or

caloric restriction (CR) diet (n = 7 per group). Bands at 50 and 100 kDa were quantified. Data were analyzed by two-tailed unpaired t tests. Bar graphs show means ± SD. Dots in each group represent biological replicates. * = $p < 0.05$, ** = $p < 0.01$, *** = $p < 0.001$, ns = not significant.

Figure 5. NCLX KD impairs starvation and rapamycin-induced autophagy. AML12 cells transfected with NCLX (siNCLX) or negative control (siNC) siRNA were analyzed by (**A**) western blots for LC3 II and (**B**) LC3 I after 1 hour exposure to either complete media (CM) or HBSS (n = 6). (**C**) Western blot analysis of LC3 II after 1 hour exposure to HBSS in the absence or presence of 100 nM Bafilomycin A1 during the last 30 min of treatment (n = 6). Data were analyzed by two-way randomized blocks ANOVA followed by Tukey's multiple comparisons test. (**D**) LC3 II net flux in siNC and siNCLX cells treated with HBSS. Data were analyzed by two-tailed unpaired t test. (**E**) western blots for LC3 II and (**F**) LC3 I after 3 hours exposure to complete media (CM) in the presence of vehicle (DMSO) or 200 nM rapamycin (n = 6). (**G**) Western blot analysis of LC3 II after 3 hours of 200 nM rapamycin treatment in the absence or presence of 100 nM Bafilomycin A1 during the last hour of treatment (n = 6). Data were analyzed by two-way randomized blocks ANOVA followed by Tukey's multiple comparisons test. (**H**) LC3 II net flux in siNC and siNCLX cells treated with 200 nM rapamycin. Data were analyzed by two-tailed unpaired t test. (**I**) Representative images and quantification of autophagosomes ($mCherry^+/GFP^+$; yellow puncta) and autolysosomes ($mCherry^+/GFP^-$; red puncta) per cell in AML12 stably expressing the mCherry-EGFP-LC3B probe, after 1 hour exposure to HBSS (n = 4). Data were analyzed by two-tailed unpaired t test. Data are presented in columns with means or means ± SD. Dots in each group represent biological replicates and paired biological replicates are represented by equally colored symbols. * = $p < 0.05$, ** = $p < 0.01$, *** = $p < 0.001$, ns = not significant.

Figure 6. NCLX inhibitor CGP 37157 suppresses starvation-induced autophagy. (**A**) Measurements of intramitochondrial Ca^{2+} levels to evaluate efflux rates after 100 µM ATP stimulation in the presence of vehicle (DMSO) or 10 µM CGP 37157 (CGP) (n = 3). (**B)** Cytosolic Ca^{2+} measurements using Fura-2 AM after stimulation with 100 µM ATP; bar graphs showing

quantifications of Ca^{2+} peaks and the half-life of one phase decay after the peak (n = 4). Data were analyzed by two-tailed paired t test. (**C)** Western blot analysis for LC3 II and (**D**) LC3 I after 1 hour exposure to either complete media (CM) or HBSS in the presence of either DMSO or 10 µM CGP (n = 6). (**E**) Western blot analysis of LC3 II after 1 hour exposure to HBSS in the absence or presence of 100 nM Bafilomycin A1 during the last 30 min of treatment (n = 6). Data were analyzed by two-way randomized blocks ANOVA followed by Tukey's multiple comparisons test. (**F**) LC3 II net flux of DMSO- and CGP-treated cells after 1 hour HBSS exposure. Data were analyzed by two-tailed unpaired t test. (**G**) Western blots for LC3 II and **(H)** LC3 I after 3 hours exposure to complete media (CM) in the presence of vehicle (DMSO) or 200 nM rapamycin and in the presence of either DMSO or 10 µM CGP (n = 6). (**I**) Western blot analysis of LC3 II after 3 hours of 200 nM rapamycin treatment in the absence or presence of 100 nM Bafilomycin A1 during the last hour of treatment (n = 6). Data were analyzed by two-way randomized blocks ANOVA followed by Tukey's multiple comparisons test. (**J**) LC3 II net flux in DMSO- and CGP-treated cells in the presence of 200 nM rapamycin. Data were analyzed by two-tailed unpaired t test. (**K**) Western blot analysis of phosphorylated 4E-BP1 in DMSO or CGP-treated cells after HBSS (n = 5) or (**L**) rapamycin (n = 3) stimulation. (**M**) Western blots for LC3 I and LC3 II in AML12 cells pre-incubated with 50 µM BAPTA-AM for 1 hour (n = 6). Data were analyzed by two-way randomized blocks ANOVA followed by Tukey's multiple comparisons test. Data are presented in columns with means or means ± SD. Dots in each group represent biological replicates and paired biological replicates are represented by equal color dots. * = $p < 0.05$, ** = $p < 0.01$, *** = $p < 0.001$, **** = $p < 0.0001$, ns = not significant.

Supplementary Figure 1. RT-qPCR analysis of AML12 cells transfected with either negative control (siNC), (**A**) MCU or (**B**) NCLX target siRNAs, 48 or 72 hours after transfection (n = 5-6). Data were analyzed by two-tailed paired t tests. (**C**) Western blot analysis of MCU levels 72 hours after siRNA transfection (n = 4). Data were analyzed by one-way randomized blocks ANOVA followed by Bonferroni's multiple comparison test. Bar graphs show mean ± SD. Dots in each group

represent biological replicates and dots of equal color indicate paired replicates. * = $p < 0.05$, ** = $p < 0.01$, *** = $p < 0.001$, ns = not significant.

Supplementary Figure 2. RT-qPCR analysis of AML12 cells transfected with either negative control (siNC), (**A**) NCLX or (**B**) MCU target siRNAs, 48 or 72 hours after transfection (n = 5-6). Data were analyzed by two-tailed paired t test. (**C**) Western blot analysis of ATG7 and (**D**) ATG12-ATG5 conjugates 72 hours after siRNA transfection (n = 4). Data were analyzed by one-way randomized blocks ANOVA followed by Bonferroni's multiple comparison test. Bar graphs show means ± SD. Dots in each group represent biological replicates and dots of equal color indicate paired replicates. * = $p < 0.05$, ** = $p < 0.01$, *** = $p < 0.001$, ns = not significant.

Supplementary Figure 3. Kinetics and quantification of proteasome activity in AML12 cells 72 hours after transfection with either negative control (siNC), MCU or NCLX target siRNAs. Analysis was performed also in the presence of 50 µg Bortezomib to confirm specificity for proteasome activity (n = 4). Data were analyzed by one-way randomized blocks ANOVA followed by Bonferroni's multiple comparison test. Bar graphs show means ± SD. Dots in each group represent biological replicates and dots of equal color indicate paired replicates. * = $p < 0.05$, ** = $p < 0.01$, *** = $p < 0.001$, ns = not significant.

Tables

Supplementary Table 1. RT-qPCR primers.

Gene	Forward (5' - 3')	Reverse (5' - 3')
Map1lc3a	ATGAGCGAGTTGGTCAAGATC	CGTCTTCATCCTTCTCCTGTTC
Map1lc3b	TTATAGAGCGATACAAGGGGGAG	CGCCGTCTGATTATCTTGATGAG
Tfeb	GCAGCCACCTGAACGTGTA	TGTTAGCTCTCGCTTCTGAGT
Atg7	CGTTGGAGTTCAGTGCTTTTG	ACCTGACTTTATGGCTTCCC
Atg5	TGAATATGAAGGCACACCCC	GGATGGACAGTGTAGAAGGTC
Atg12	ACCATCCAAGGACTCATTGAC	TGCAGGACCAGTTTACCATC
Mcu	ACTCACCAGATGGCGTTCG	CATGGCTTAGGAGGTCTCTCTT
Slc8b1	TGTCACCTTCCTGGCCTTTG	CACCCCTGCACCAAACAGA
Actb	TCACTATTGGCAACGAGCG	AGGTCTTTACGGATGTCAACG
Hmbs	CAGCTACAGAGAAAGTTCCCC	AGGACGATGGCACTGAATTC
B2m	CTGGTCTTTCTATATCCTGGCTC	TGCTTGATCACATGTCTCGATC

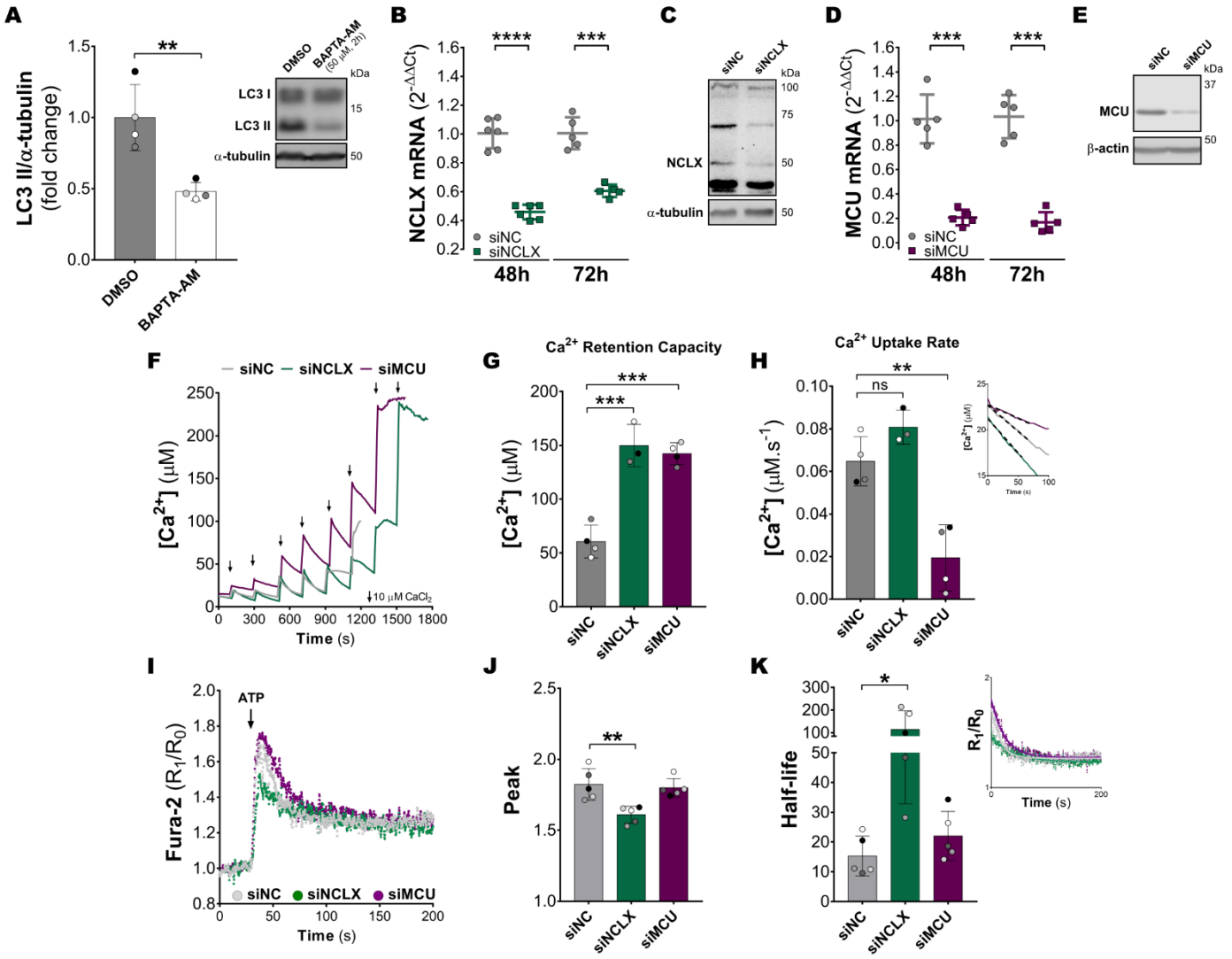

Ramos et al., Figure 1

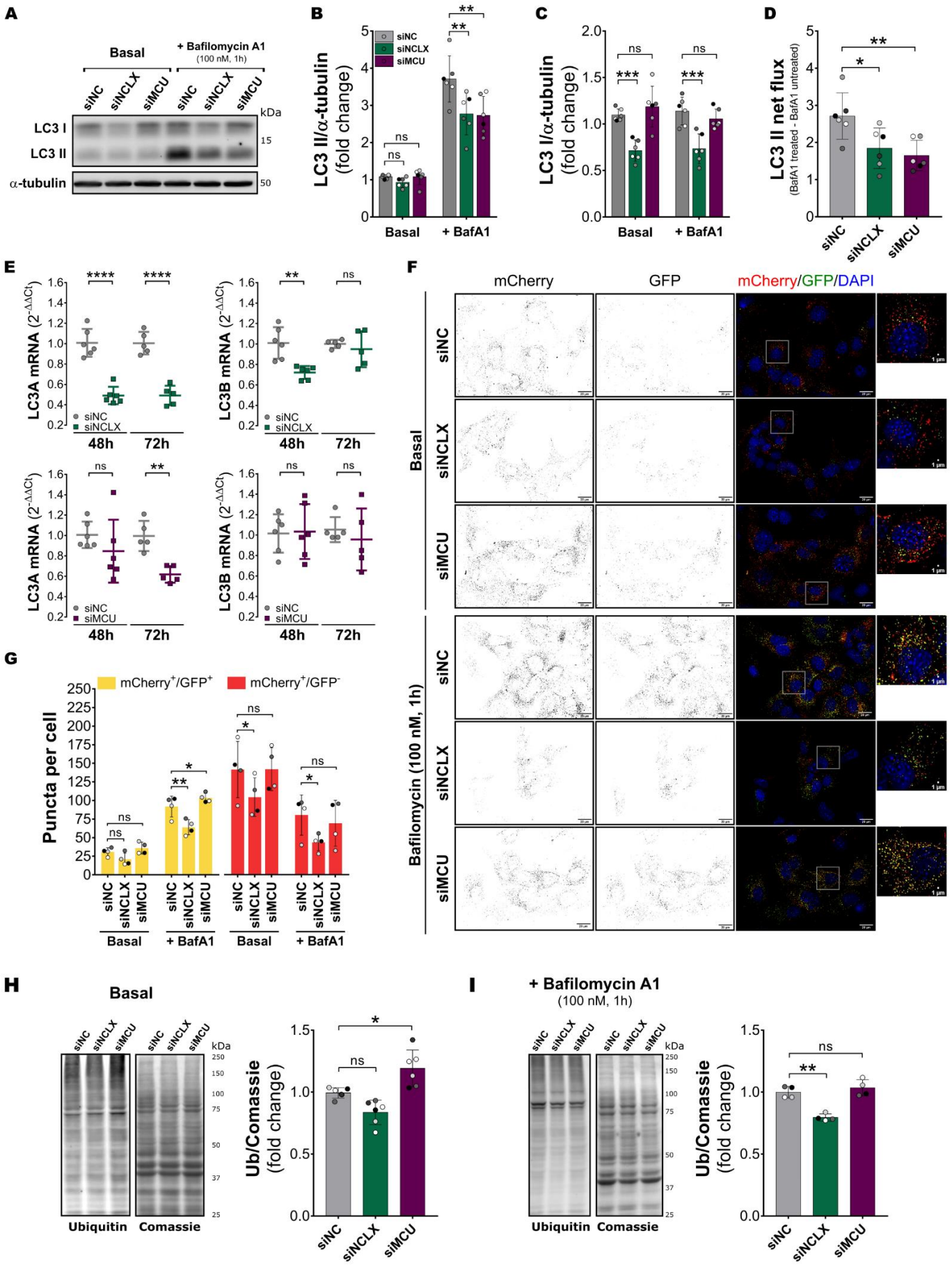

Ramos et al., Figure 2

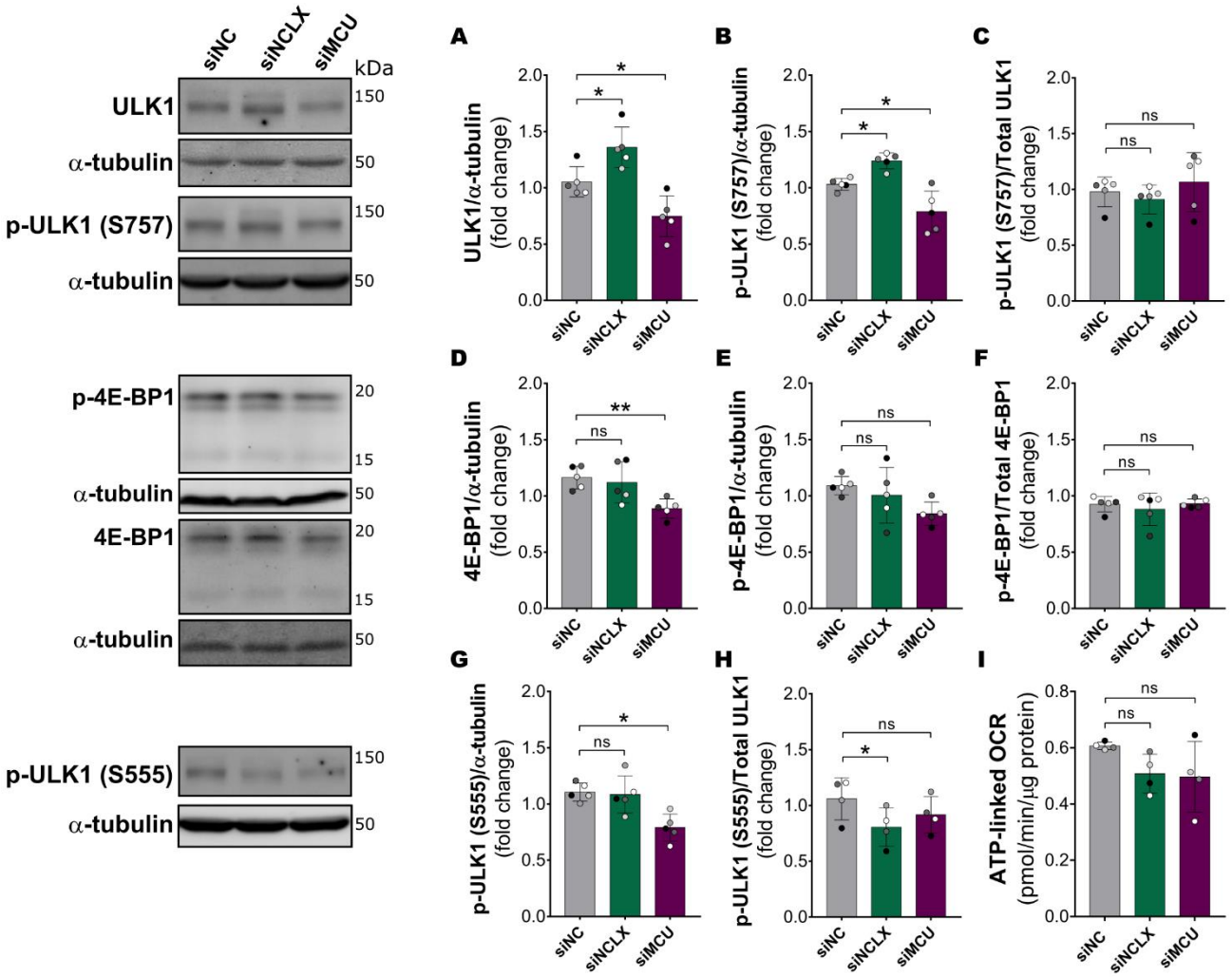

Ramos et al., Figure 3

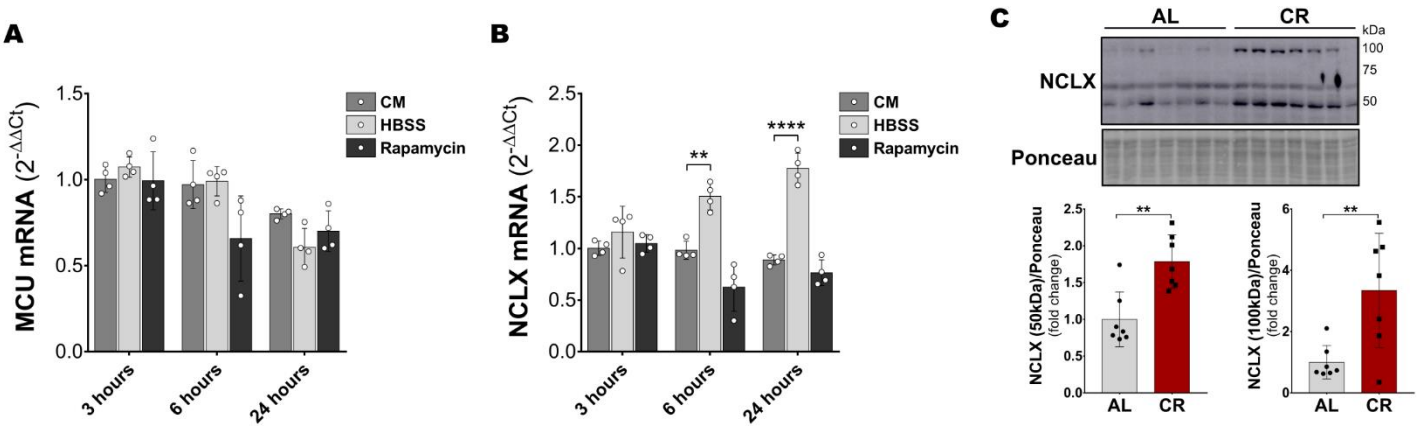

Ramos et al., Figure 4

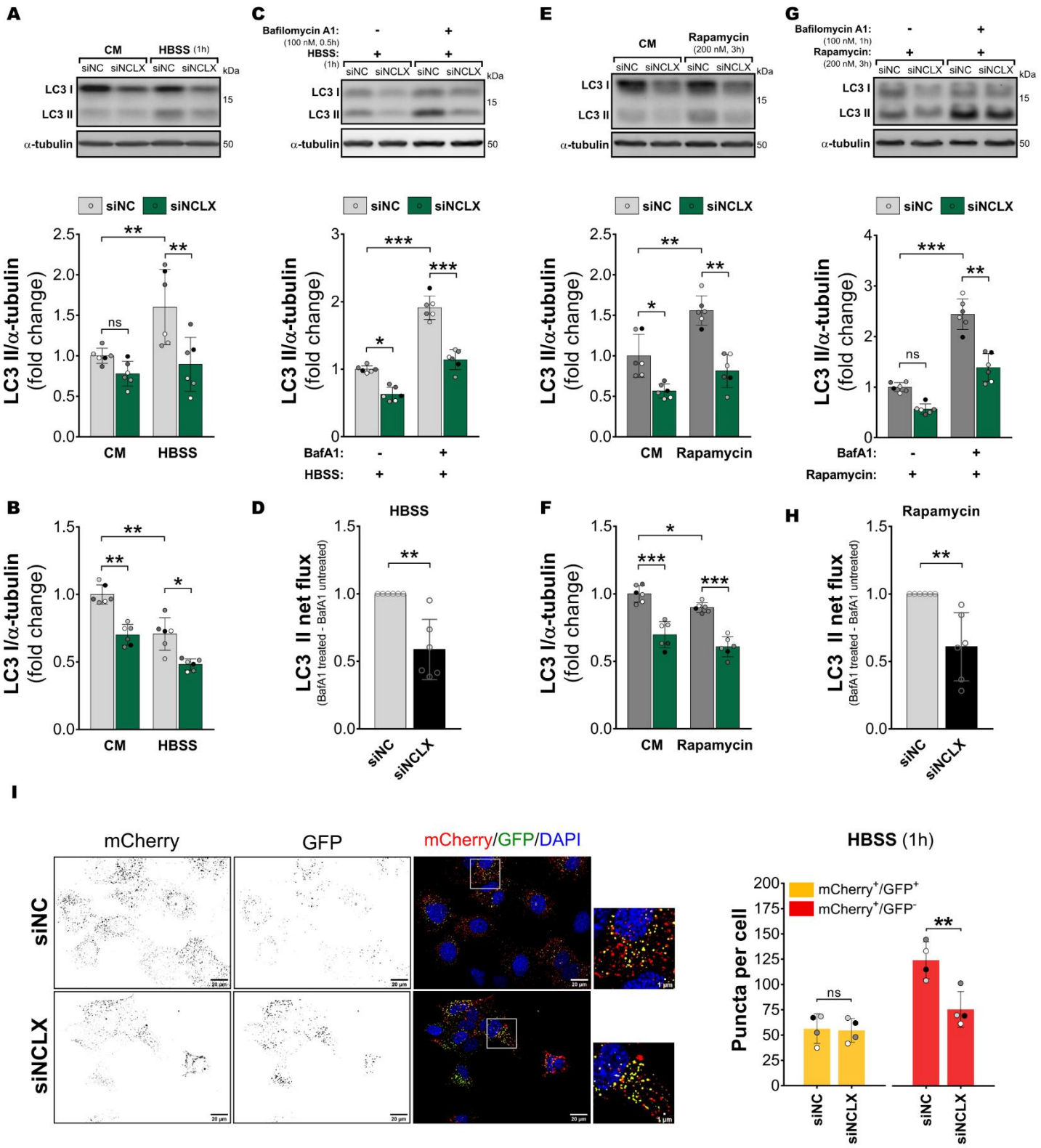

Ramos et al., Figure 5

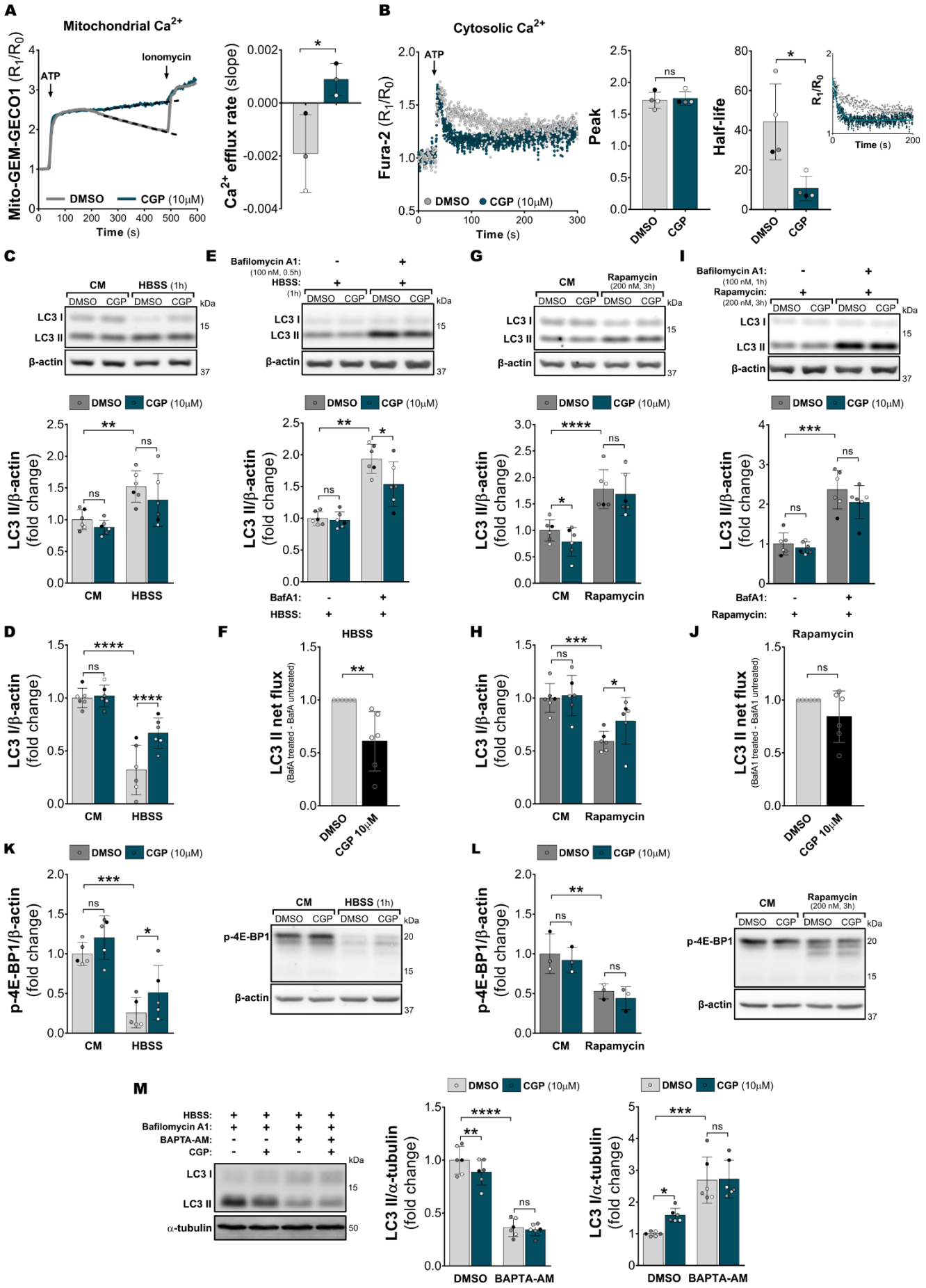

Ramos et al., Figure 6

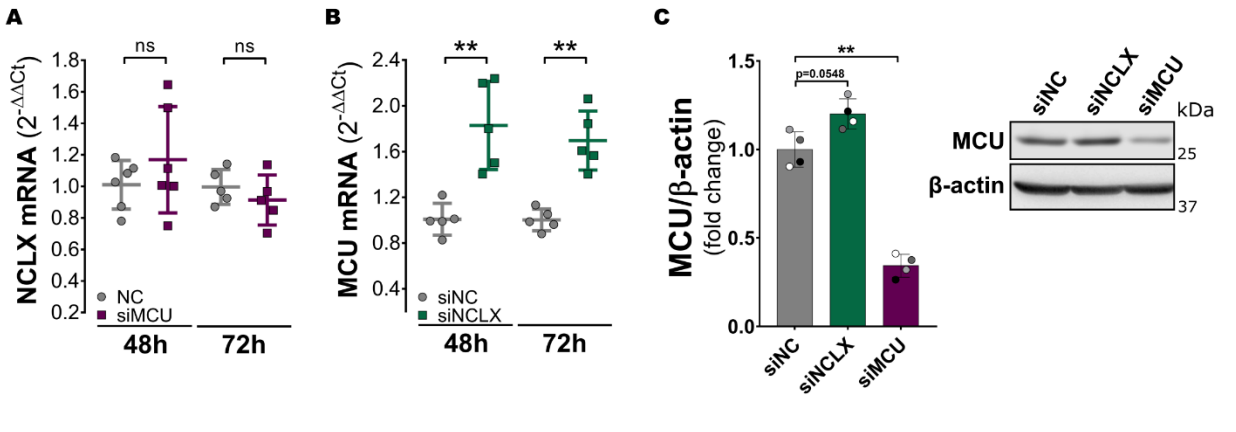

Ramos et al., Supplementary Figure 1

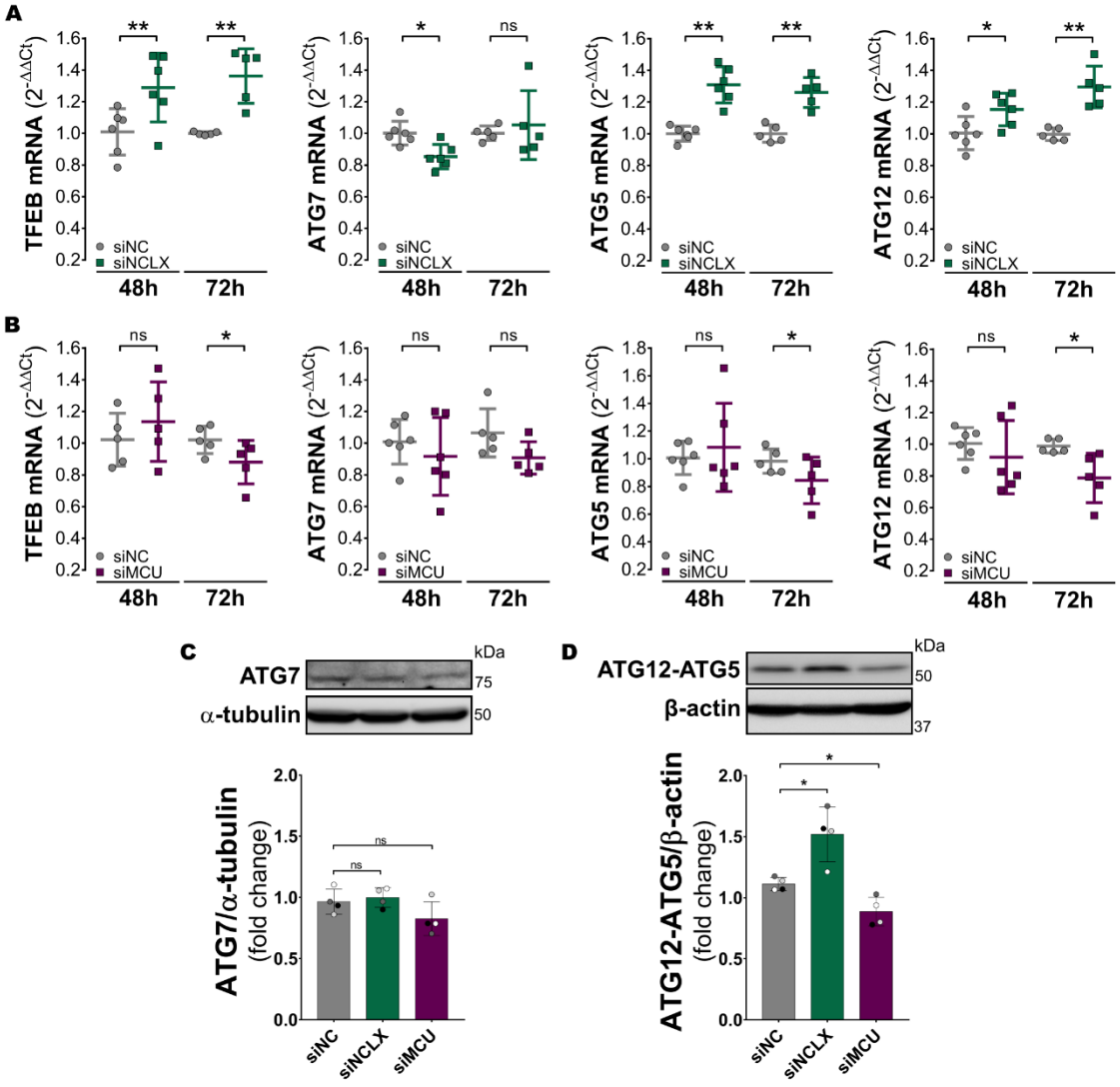

Ramos et al., Supplementary Figure 2

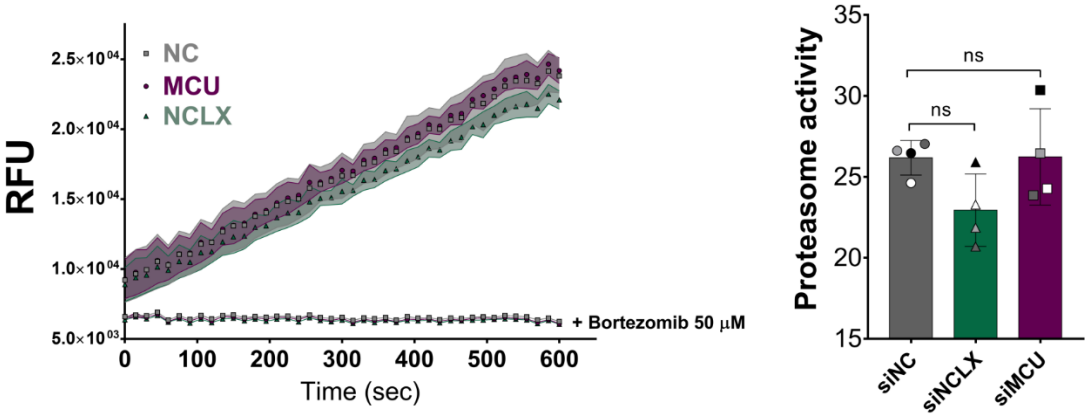

Ramos et al., Supplementary Figure 3